ACS OMEGA

http://pubs.acs.org/journal/acsodf

Article

Green Biosynthesis of Tin Oxide Nanomaterials Mediated by Agro-Waste Cotton Boll Peel Extracts for the Remediation of Environmental Pollutant Dyes

Boya Palajonnala Narasaiah,[#] Pravallika Banoth,[#] Arya Sohan, Badal Kumar Mandal, Angel G. Bustamante Dominguez, Luis De Los Santos Valladares,* and Pratap Kollu*

Cite This: *ACS Omega* 2022, 7, 15423−15438

Read Online

ACCESS | Metrics & More | Article Recommendations

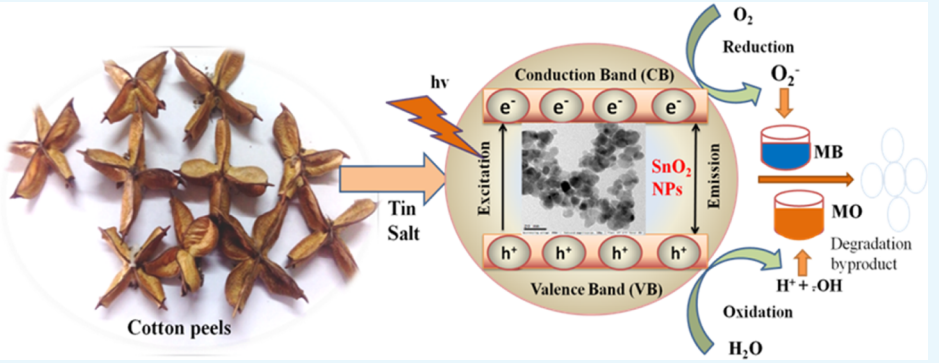

ABSTRACT: The sustainable synthesis of metal oxide materials provides an ecofriendly and more exciting approach in the domain of a clean environment. Besides, plant extracts to synthesize nanoparticles have been considered one of the more superior ecofriendly methods. This paper describes the biosynthetic preparation route of three different sizes of tetragonal structure SnO_2 nanoparticles (SNPs) from the agro-waste cotton boll peel aqueous extract at 200, 500, and 800 °C for 3 h and represents a low-cost and alternative preparation method. The samples were characterized by X-ray diffraction, Fourier transform infrared spectrophotometry, ultraviolet−visible absorption spectroscopy, high-resolution transmission electron microscopy (HR-TEM), and energy-dispersive X-ray spectroscopy. Surface area and porosity size distribution were identified by nitrogen adsorption−desorption isotherms and Brunauer−Emmett−Teller analysis. The photocatalytic properties of the SNP samples were studied against methylene blue (MB) and methyl orange (MO), and the degradation was evaluated with three different size nanomaterials of 3.97, 8.48, and 13.43 nm. Photocatalytic activities were carried out under a multilamp (125 W Hg lamps) photoreactor. The smallest size sample exhibited the highest MB degradation efficiency within 30 min than the most significant size sample, which lasted 80 min. Similarly, in the case of MO, the smallest sample showed a more superior degradation efficiency with a shorter period (40 min) than the large-size samples (100 min). Therefore, our studies suggested that the developed SNP nanomaterials could be potential, promising photocatalysts against the degradation of industrial effluents.

1. INTRODUCTION

Over the last years, the novel synthesis of nanomaterials such as metal, metal oxide, and metal sulfide nanoparticles have gained much attention. Metal, metal oxide, and their composites have become an exciting area in nanoscience and technology due to the many applications in versatile fields and even proven promise in human life aspects.[1] Synthesis of nanoparticles through eco-friendly routes attracted much awareness in recent years because of its environment friendly nature, that is, nontoxic to the environment, reaction process, short time, low temperature, and safe, mild reaction conditions.[2] However, modifying the surface area of the nanoparticles through the natural reducing and capping agents remains challenging. Nevertheless, nanoparticles can be generated by green chemical agents that are plant extracts that possess even higher stability.[3] The green process synthesis of metal oxide nanoparticles, particularly tin oxide nanomaterials using plant extract, is an alternative method to the chemical synthesis that could control the chemical toxicity to the environment and control the size

Received: December 16, 2021
Accepted: March 17, 2022
Published: April 26, 2022

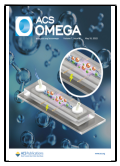

© 2022 The Authors. Published by American Chemical Society

https://doi.org/10.1021/acsomega.1c07099
ACS Omega 2022, 7, 15423−15438

and shape of the nanomaterials.[4] State of the art shows the possibilities of synthesis nanomaterials in an aqueous medium with reducing agents that counts the hydroxyl group of polyphenols that possess the stabilizing/capping agents without using hazardous chemicals.[5] Moreover, green synthesized nanomaterials are gaining interest in the research fields, environmental sciences, synthetic chemistry, nanobiotechnology, and material chemistry, respectively.[6] Among various nanomaterials, SnO_2 nanomaterials are considered an alternative source for degradation of water purification/environmental pollutants because they possess outstanding UV light absorption and generate reactive oxygen species (ROS) that lead to the degradation of environment pollutant dye molecules.[7,8]

Tin oxide nanoparticles (SnO_2 NPs) are widely used in several fields such as photocatalytic activity, energy storage application, and organic transformation used as catalysts in various fields.[9] The literature reports the synthesis of SnO_2 NPs (SNPs) through multiple methods. Nejati-Moghadam et al. (2015) reported the production of SnO_2 nanostructures by the precipitation method,[10] Ling Zhang et al. (2018) reported cubic sub-micron SnO_2 particles for the reduction of nitrogen to sustainable process for scalable NH_3 synthesis with less energy consumption,[11] and Haspulat et al. (2020) have synthesized SnO nanoparticles in the presence of Triton-X 100 (TX-100) surfactant assisted via the hydrothermal method.[12] Maharajan et al. (2020) reported a nano-Rattle SnO2@carbon composite by melt diffusion method/thermal decomposition methods for the material for high-energy Li-ion batteries.[13] Karmaoui et al. (2018) studied the band gap properties and structural study of SNPs and synthesized a one-step process by the sol gel method.[14] Zhu et al. (2019) reported ultrafine SNPs (diameter 2−4 nm) fabricated on the surfaces of g-C_3N_4 material through the combination of the hydrothermal method and ball milling in order to improve the dispersion of SnO_2 NPs as well as to strengthen the bonding between SnO_2 and g-C_3N_4.[15] These methods are reported to be effective for controlling the shape and size of the nanoparticles. However, all these methods require high temperature, high cost, and environmentally hazardous chemical precursors during synthesis processes. Therefore, environmentally friendly, low-cost, and straightforward production is preferred.

The potential nanomaterials synthesizing through physical and chemical methods are expensive and require high pressure, temperature, and energy. They include prolonged reactions and required toxic reactants and solvents, which are potentially hazardous to the environment. Hence, there is a continuous demand for developing new techniques for nanomaterials synthesis without the above drawbacks. Green synthesis has been adopted nowadays as the best alternative way to overcome the methods mentioned above to synthesize nanomaterials because of several advantages such as a fast and straightforward reaction process, inexpensive approach, environmentally eco-friendly to nature, reduction of metal ions to metal nano, and use of less toxic and hazardous chemicals. The synthesis of metal oxide nanomaterials through plant extracts has turned very promising because it allows both reducing and capping agents.[16] In fact, plant extracts have various phytochemical constituents, that is, secondary metabolites such as alkaloids, terpenoids, flavonoids, antioxidants, and amino acids, respectively, which exist in fruits, peels, seeds, and leaves that permit the replacement of the traditional toxic chemicals for the synthesis of nanomaterials.[17] Diallo et al. (2016) reported the preparation of n-type SNPs by a green chemistry process using Aspalathus linear natural extract as an effective chelating agent. The obtained SNPs exhibited photocatalytic degradation of methylene blue (MB), Congo red, and Eosin Y.[18] Matussin et al. (2020) also reported plant-extract-mediated SNPs.[19] Singh et al. (2019) synthesized SnO_2 NPs through pomegranate leaves (*Punica Granatum*), and the obtained SnO_2 NPs (20 nm) showed 91.5% photodegradation efficiency of MB dye under direct sunlight within 240 min.[20] Bhattacharjee et al. (2015) developed a green process of SnO_2 quantum dots using the amino acids aspartic and glutamic as reducing agents and used for the photocatalyst in the degradation of Rose Bengal and Eosin Y dye under direct sunlight.[21] Sinha et al. (2017) green fabricated sphere-shaped Ag−SnO_2 nanocomposites (9 nm) employing stem extracts of saccharin officinarum and used as a photocatalyst and prospective antibacterial and antioxidant agents.[22] Sudhaparimala et al. (2016) reported coupled semiconductor SnO_2−ZnO NPs using the assisted gel of aloe vera plants as the medium. They studied the photocatalytic activity of the organic dye methyl orange (MO) degradation in the presence of visible light. They also studied the antibacterial activity of staphylococcus aureus and *Escherichia Coli* growth at the microgram level.[23]

Currently, photocatalysis applications for addressing environmental issues such as environmental pollution and energy crises have attracted more and more attention and gradually become a research hotspot. The most common pollutants identified in urban and industrial areas are volatile organic compounds such as toluene, benzaldehyde, benzyl alcohol, and chlorinated derivatives.[24] Volatile organic compounds are dangerous for human health, and they are toxic, mutagenic, and carcinogenic to all human beings. Nowadays, research has mostly been focused on the toxicity of volatile organic compounds sources or the degradation conditions rather than the byproducts generated during the treatment procedures.[25] The drawback of traditional methods such as absorption, incineration, and condensation used for removing volatile organic compounds from pollutants is that they are costly, have a short life, and lead to the production of secondary pollutants.[26] Some approaches have been devised recently to solve the problem. Photocatalysis is a promising technology for purifying wastewater and textile dyes under visible/ultraviolet light irradiation. For example, Cu−Fe_2O_3/Ni−ZnO nanoplate is an excellent photocatalyst for the degradation of environmental pollutants in visible light. It allows the mineralization of CO_2 and water molecules.[27] The photocatalyst activity of nanoparticles mainly depends on their high surface area, size, shape, and less band gap energy.[28] Tuan et al. (2019) noticed that the photocatalyst activity of SnO_2/rGO nanocomposites depends on their morphology, structure, and size.[29] Jiang et al. (2021) studied the anode materials for the degradation of organic pollutants by anodic oxidation.[30] Yuanyuan et al. (2018) estimated the degradation of methyl blue (MB) and Rhodamine B (RhB) by the SnO_2 nanoparticle photocatalyst in more than 90% for under UV light irradiation within 50 min and 270 min.[31] Huang et al. (2018) prepared a tetragonal phase $Bi_2O_2CO_3$ catalyst and reported its photocatalytic behavior with the degradation of MO dye under visible light conditions.[32] They also prepared Cerium-based hybrid nanorods (CN-600 to CN-800) photocatalyst; however, the CN-700 catalyst displays a degradation efficiency of 100% for MB in aqueous solution in 90 min.[33]

The present work reports the green production of photocatalyst of tetragonal structure SNPs of different sizes (2−13 nm) from eco-friendly nature, cost effective manner using Agro-

https://doi.org/10.1021/acsomega.1c07099
ACS Omega 2022, 7, 15423−15438

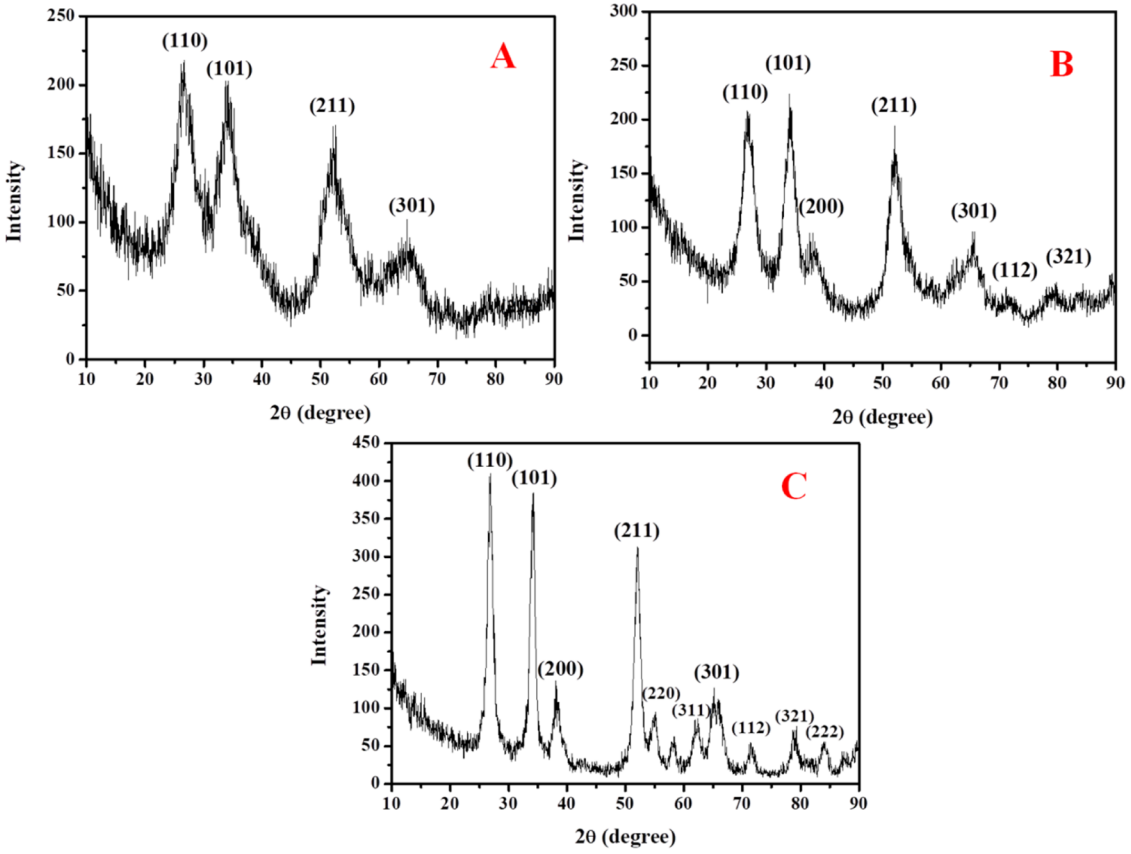

Figure 1. XRD pattern of sample SNPs: SNPs-200 °C (A), SNPs-500 °C (B), and SNPs-800 °C (C).

waste cotton boll peels with tin Chloride di-hydrate as a precursor. The prepared tetragonal structure SnO_2 photocatalyst nanoparticles were characterized by X-ray diffraction (XRD) technique, high-resolution transmission electron microscopy (HR-TEM), UV−visible diffuse reflectance spectroscopy (UV−vis DRS), and surface area analyzed by Brunauer−Emmett−Teller (BET). The tetragonal structure SnO_2 photocatalyst offered an enhanced catalytic activity to degrade MB and MO dyes under UV light irradiation.

2. EXPERIMENTAL PROCEDURE

2.1. Material and Methods. Tin chloride di-hydrate ($SnCl_2{\cdot}2H_2O$), MB, and MO were purchased from Sigma Aldrich to synthesize the SNP samples. All other chemicals and reagents used analytical grade with no purification, and double-distilled water was used as a solvent. Agro-waste cotton peels were collected near the Tungabhadra River, Mantralayam Road, Kurnool District, Andhra Pradesh, India.

2.2. Preparation of Agro-Waste Cotton Peel Extracts. Freshly collected peels were washed 2−3 times under running tap water, followed by sanitizing with Milli-Q water one time and then dried at room temperature under dust-free conditions for 1 week. The preparation followed a similar way reported by Balaji Reddy et al. (2017) to synthesize metal oxide nanoparticles using *Eucalyptus globulus* leaf.[34] The dried peels were ground into powder through an electric mixer and sieved by a 100 mesh sieving net. About 3 g of powder was added to 100 mL of de-ionized water and kept for boiling on a water bath at 80 °C for 30 min to prepare the aqueous extract. Eventually, the extract was cooled at room temperature, filtered through a Whatman no.1 filter paper, and stored at 4 °C in a refrigerator.

2.3. Synthesis of Tin Oxide (SnO_2 NPs) from Agro-Waste Cotton Peel Extract. About 0.329 g of Tin chloride di-hydrate ($SnCl_2{\cdot}2H_2O$) (0.05 M) was dissolved in 30 mL of double-distilled water and subsequently 30 mL of agro-waste cotton peel aqueous extract was added drop-wise while thoroughly stirring at 80 °C for 3 h. The color of the solution changed from light yellow to brown color after 30 min because of the heating process. Then, the mixture was cooled at room temperature and subsequently centrifuged for 30 min at 6000 rpm. The residue was carefully collected and washed three times with absolute ethanol, following washing with double-distilled water and eventually dried on the hot plate at 60 °C. The resulting dried powder followed calcination at 200 °C for 3 h inside a muffle furnace. That sample was labeled as tin oxide (SnO_2) nanoparticles (SNPs-2). A similar procedure was used to prepare additional samples, once synthesized and calcined at 500 °C, labeled as SNPs-5, and another at 800 °C (labeled as sample SNPs-8) for 3 h inside a muffle furnace.

2.4. Characterization of the SnO_2 Nanoparticles. A X-ray powder diffractometer, Bruker D8, was used to measure the SNPs samples by X-ray diffraction. The data were recorded in the range of 2θ values from 10 to 90° with a scanning rate of 4° min^{-1} by using the Cu-Kα radiation with a λ_{max} of 1.54 Å. The morphology and size of the synthesized SNPs were inspected by dispersing the SNP samples onto Cu grids through HR-TEM (Model: JEM 2100 USA JEOL) with 0.1 nm resolution and an acceleration voltage of 200 keV. The TEM equipment also provided information about the elemental composition of the samples by energy-dispersive X-ray (EDX) analysis. The optical properties of the synthesized SNP samples were also analyzed by using a Shimadzu (model UV-2450) UV−visible spectropho-

https://doi.org/10.1021/acsomega.1c07099
ACS Omega 2022, 7, 15423−15438

tometer at room temperature. The bang gap calculations assumed the absorption band. The functional groups in the cotton peel agro-waste aqueous extract SNP samples were analyzed using FT-IR (Fourier transform infrared) spectroscopy. Functional groups determined in purified dried SNP samples using a Shimadzu IR AFFINITY-1 against the agro-waste cotton peel aqueous extract. However, pelted took control under similar instrumental conditions using JASCO FT-IR in the wavenumber range 500−4000 cm^{-1} at a resolution of 4 cm^{-1} using potassium bromide pellets in the diffuse reflectance mode. Quanta chrome nova-1000 autosorb-1 instrument was used to determine the surface area and pore diameter through nitrogen adsorption−desorption isotherms.

2.5. Photocatalytic Activity of SNP Samples. The SNP samples were used as a photocatalyst to degrade the MB and MO dyes under UV light irradiation. The present investigation was performed with a Heber photoreactor having multilamp UV lamps (254 nm) with a low pressure of 125 W under continuous stirring. The experiment was carried out by loading 0.02 g of SNP samples with 60 mL of MB dye solution (concentration 10 mg/L) into a quartz tube (100 mL capacity) and then followed by continuous stirring, without disturbance, under the dark condition for 50 min without UV-light exposure to obtain the constant equilibrium. After getting the stable equilibrium, the final solution was exposed with UV light radiations at 125 W, 254 nm, and regular time intervals. The sample was collected in an Eppendorf tube (2 mL capacity) and centrifuged. The degraded de-colorization solution was monitored by UV−vis spectro-photometer analysis to record the de-colorization solution's absorbance, scanned at 200−800 nm. The catalyst was then recollected after complete de-colorization of MB dye molecules through centrifugation. We also recycled it to check the stability and reusability of the SNP catalyst. The same procedure was repeated for the MO dye degradation and all other samples (SNPs-5 and SNPs-8) to degrade MB and MO dyes. We also studied the effects of varying catalysts and dye concentration for MB and MO degradation of dyes. Thus, the degradation of the samples was recorded by UV−vis spectroscopy.

3. RESULTS AND DISCUSSION

3.1. Determination of Crystalline Nature from XRD-Analysis of SNP Samples. XRD patterns of the samples SNPs-2, SNPs-5, and SNPs-8 are shown in Figure 1 and analyzed to estimate the crystal structure and crystallinity of the nanomaterials. The diffraction pattern of sample SNPs-2 represents reflections at 2θ = 26.53, 34.38, 52.12, and 65.27° which correspond to the diffraction peaks *hkl* values of lattice planes (110), (101), (211), and (220), respectively (see Figure 1A). The confirmed diffraction pattern corresponds to the tetragonal structure of SnO_2 NPs at 200 °C, which matches the standard Match3 software (JCPDS card no: 96-210-4744). Because the XRD pattern presents monophasic diffraction, that confirms the purity of the SNP-2 nanomaterials. Figure 1B presents the XRD pattern of the SNP-5 sample with 2θ reflections at 26.96, 34.52, 38.22, 52.16, 65.68, 71.53, and 78.72° which attributes to the Miller indices reflecting planes (110), (101), (200), (211), (301), (112), and (321), respectively, and with the tetragonal structure after annealing at 500 °C (JCPDS card no: 96-210-4744). However, there are no impurity peaks in the RDX pattern, which indicates the purity of SNP-5.

The XRD pattern for sample SNPs-8, shown in Figure 1C, presents 2θ reflections at 26.82, 34.29, 38.26, 52.27, 54.77, 62.11, 65.78, 71.49, 78.86, and 83.69° which are characteristic diffraction peaks of *hkl* planes (110), (101), (200), (211), (220), (311), (301), (112), (321), and (222), respectively. Therefore, the noticed XRD patterns confirm the tetragonal structure of the SNPs-8 sample and match the standard Match3 software (JCPDS card no: 96-210-4755). The results concluded that all the SNP samples are tetragonal structures in pure phase so that the activity of SNP samples depends on its crystallinity nature.

Table 1 summarizes the results given by XRD: the full width at half-maximum (fwhm), inter-planar distance (d) values, and crystallite sizes. The crystallite sizes were calculated to be 4.7, 9.7, and 14 nm for the SNPs 2, 5, and 8, respectively, meaning that the annealing process plays a significant role in the crystallization and changes the fwhm values. The increase of temperature influences in the diffraction intensity and reduces the fwhm values, attributed to the systematic arrangement of atoms on the crystal system. Therefore, increasing the annealing temperature gradually increases the particle size because of oxygen vacancies, originated by atomic diffusion, lattice strains, and crystal lattice defects, which causes the crystallite size to increase. The SNP samples crystallite size could be calculated according to the following Scherrer formula equation I

$$D = k\lambda/\beta \ \mathrm{Cos}(\theta) \quad \text{(I)}$$

Here, D is the crystallite size, k is the Scherrer's coefficient (0.891), λ is the X-ray wavelength, θ is the Bragg angle, and β is the fwhm intensity (in radians). Note that the crystallite size is obtained or defined as the measurement of the diffracting crystallite size of the samples that are not equal to the particle size because they exhibit polycrystalline aggregates. Estimation of the crystallite sizes and interplanar distance (d) values of the SNP samples planes fitted with Scherrer's equation are listed in Table 1. Therefore, calculated average crystallite sizes of sample SNPs-2 at 200 °C, sample SNPs-5 at 500 °C, and sample SNPs-8 at 800 °C are 4, 9, and 14 nm, respectively. Similar results have been obtained by Osuntokun et al. (2017) using the leaf extract of *Brassica oleracea* L. var. botrytis which results in SNPs with crystallite sizes 3.6−6.3 nm.[35]

3.2. Size and Morphology Identified by HR-TEM Analysis. The size, morphology, *d*-spacing, elemental composition, and crystalline/amorphous nature of the SnO_2 samples were inspected by HR-TEM as shown in Figures 2−4. The HR-TEM images of sample SNPs-2 at different magnifications, selected area electron diffraction pattern (SAED), particle size distribution, and EDX spectra are presented in Figure 2A−F. Figure 2A,B displays the micrographs of sample SNPs-2 at different magnifications, and the size identified by the Image J software ranges 2.92−4.59 nm so that the average diameter (AD) is 3.97 nm. Moreover, the interplanar distance representing the d-spacing is 0.262 nm which is characteristic for the reflection plane (101), as shown in Figure 2C. The diffraction rings in the SAED pattern shown in Figure 2D expose the amorphous nature, corresponding to the amorphous SnO_2 component of the SNPs-2 noticed from the respective XRD background above. The identified elemental composition of the SNPs-2 sample, determined by the EDX spectrum in Figure 2E, reveals weight % and atomic % of tin and oxygen: 86.59 and 13.41 weight % and 46.53 and 53.47 atomic %, respectively, and no other impurities are found. Therefore, the obtained results confirm that the SNPs-2 sample also contains amorphous SnO_2 without impurity. Figure 2F presents the particle size histogram, where the particle size distribution is around 2.92−4.59 nm with

https://doi.org/10.1021/acsomega.1c07099
ACS Omega 2022, 7, 15423−15438

Table 1. Structure and Geometric Parameters of SNP Samples of Diffraction Study

SNPs	lattice plane	2θ	fwhm value	d-spacing (Å)	Cos(θ)	crystallite size (nm)
SnO_2 NPs at 200 °C	(110)	26.53	2.044	3.46	0.9733	4.2
	(101)	34.38	2.557	2.63	0.9553	3.4
	(211)	52.12	2.587	1.84	0.8983	3.6
	(220)	65.27	1.273	1.45	0.8421	7.8
average size						4.7
SnO_2 NPs at 500 °C	(110)	26.96	1.754	3.37	0.9724	4.9
	(101)	34.52	0.717	2.68	0.9549	12.1
	(200)	38.22	0.748	2.43	0.9448	11.8
	(211)	52.16	0.972	1.86	0.8981	9.5
	(220)	65.68	0.970	1.41	0.8401	10.2
average size						9.7
SnO_2 NPs at 800 °C	(110)	26.82	0.857	3.35	0.9727	10
	(101)	34.29	0.670	2.67	0.9555	13
	(200)	38.26	0.493	2.48	0.9447	17.8
	(211)	52.27	0.936	1.75	0.8977	9.9
	(220)	54.77	0.647	1.79	0.8879	14.5
	(311)	62.11	0.606	1.54	0.8566	16
	(301)	65.78	0.526	1.47	0.8397	18.8
	(321)	78.86	0.847	1.26	0.7724	12.7
average size						14

an AD of 3.97 nm and the standard deviation (SD) is approximately 0.07 nm.

Figure 3A−F shows the HR-TEM, EDX spectrum, SAED pattern, and particle size distribution of the SNPs-5 samples. Figure 3A,B presents TEM micrographs at different magnifications showing that the size of the particles ranges from 5.2 to 12.8 nm, and the AD is 8.4 nm. The interplane distance is around 0.27 nm, characteristic of the reflection plane (101) as represented in (Figure 3C). The circular rings existing in the SAED pattern (see Figure 3D) correspond to the poly-crystallinity nature of the SNPs-5 sample. The elemental composition of the SNPS-5 sample from the EDX spectrum (see Figure 3E) reveal tin and oxygen in atomic % and weight % are as follows: 48.76, 51.24 and 87.60, 12.40% respectively, which indicates that the polycrystalline SNPs-5 sample has no impurities. The particle size distribution is shown in Figure 3F, where particles range from 5.2 to 12.9 nm. The average particle size diameter is 8.5 nm, and the SD is around 0.4 nm.

Figure 4A−F displays the HR-TEM, SAED pattern, EDX spectrum, and particle size distribution of the SNPs-8 sample. Figure 4A,B presents different magnification TEM micrographs showing particle sizes between 15.6 and 7.7 nm with an AD of 13.4 nm. Figure 4C reveals that the inter plane distance (d) is 0.27 nm, which agrees with the respective XRD results and corresponds to the diffraction reflection plane (101). The circular radiant spots in the SAED pattern (see Figure 4D) confirms the poly-crystallinity nature of the sample. Figure 4E shows the EDX spectrum revealing the elemental composition as tin and oxygen in atomic % and weight %: 53.84, 46.16 and

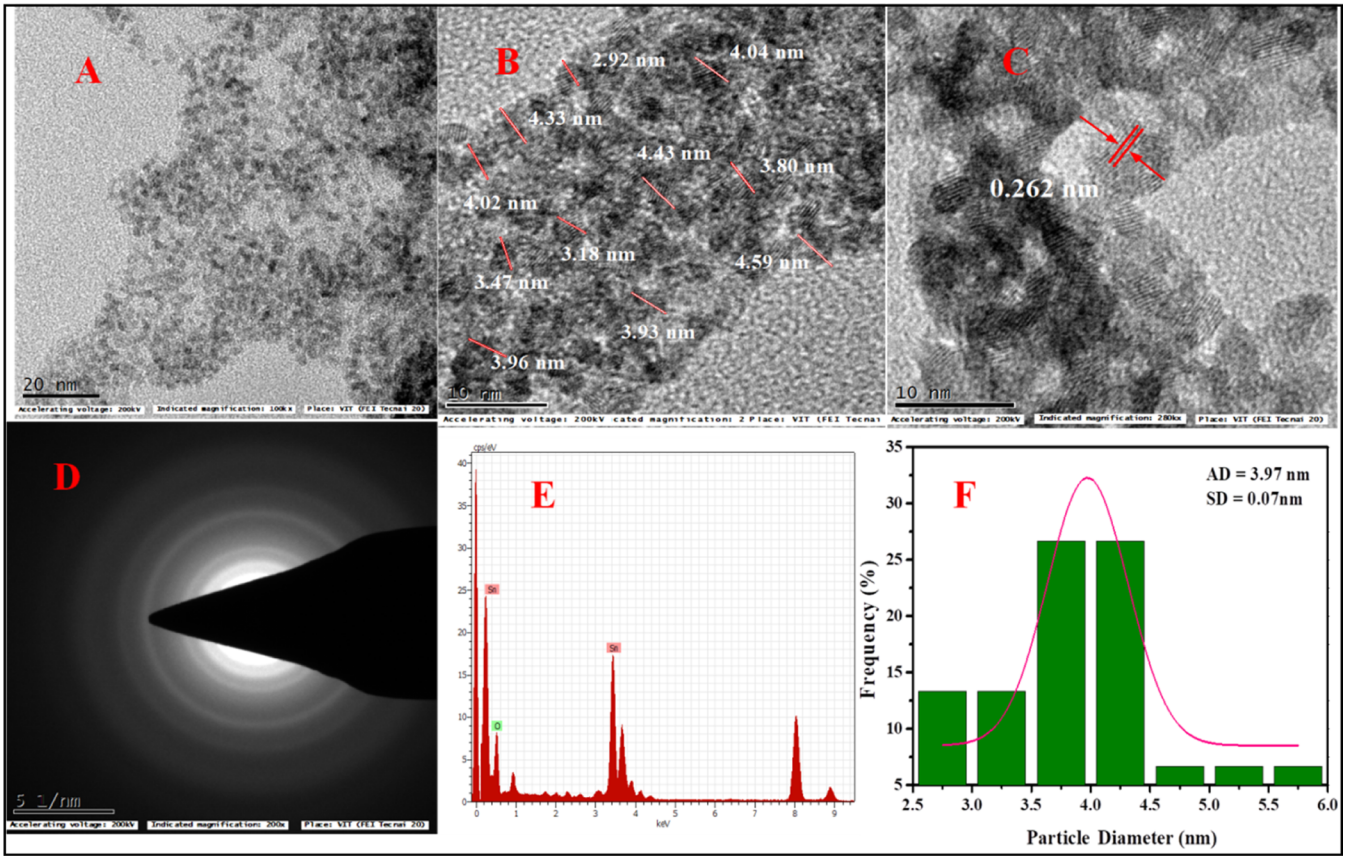

Figure 2. HR-TEM of sample SNPs-2 at annealing at 200 °C; (A,B) different scale magnifications (20 and 10 nm), (C) inter planar d-spacing, (D) SEAD pattern, (E) EDX micrograph, and (F) particle size distribution of the histogram.

https://doi.org/10.1021/acsomega.1c07099
ACS Omega 2022, 7, 15423−15438

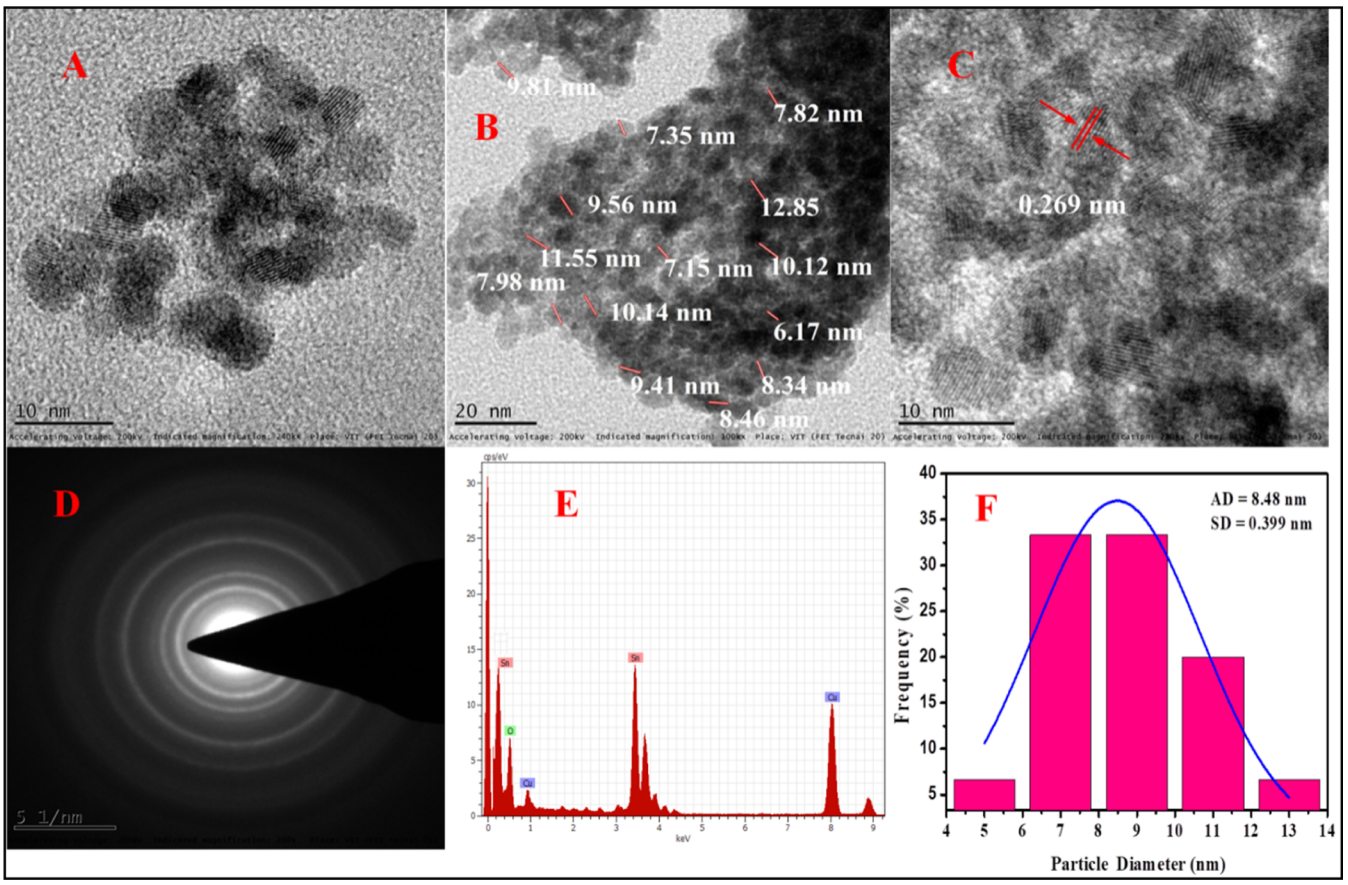

Figure 3. HR-TEM of sample SNPs-5 at annealing at 500 °C; (A) 10 nm scale magnification, (B) 20 nm scale magnification, (C) inter planar *d*-spacing, (D) SEAD pattern, (E) EDX micrograph, and (F) particle size distribution of the histogram.

89.87, 10.13%, respectively, which leads to the purity of the SNPs-8 sample. The histogram of the particle size distribution is shown in Figure 4F, where particles range around 15.6−7.7 nm, giving the average particle size diameter (AD) of 13.4 nm and SD is 0.8 nm. Similarly, Ma et al. (2020) reported SNPs obtained by the precipitation method to be in the range of 20−80 nm and an average particle size around 40 nm.[36]

The TEM results of three samples (SNPs-2, SNPs-5, and SNPs-8) demonstrate the strong influence of the temperature on the size of the SnO_2 nanomaterials. Increasing the annealing temperature may lead to defects in the crystal system and subsequently regulate the arrangement of atoms in the unit cell resulting in the rise of the size of the nanoparticles and the crystallinity, as confirmed by XRD above. From the results, we concluded that the annealing process could control the size of the NPs.

3.3. Identification of Functional Groups on the Surface of the SNPs by FTIR Analysis. FTIR analysis is a well-known technique to determine the functional groups in the cotton peel aqueous extract and the capping of biomolecules on the surfaces of the SNPs based on the vibrational stretching of functional groups. Figure 5A describes the FTIR spectrum of the agro-waste cotton peel aqueous extract recorded in the range 4000−500 cm^{-1}. In the defined spectrum, the bands located around 3346.78, 3257.63, 1737.86, 1606.64, 13346.78, 1105.97, and 921.58 cm^{-1} are associated with the stretching vibration of the hydroxyl (−OH) group (indicating the existence of polyphenols in the plant extract); stretching vibration of the aromatic amine (−N−H) group; stretching vibration of the carbonyl (−C═O) group; bending vibration of the amide (−N−H) group corresponding to nitrogen and hydrogen vibrations; vibration of the nitro (−N−O) group; ether group of (−C−O−C−); and bending vibration of aliphatic carbon and hydrogen (−C−H) groups, respectively. Similarly, Arumugam et al. (2021) reported various biomolecules in *Syzygium cumini* (Java plum) aqueous extract detected from the FTIR technique.[37]

Figure 5B displays the FTIR spectrum of the SNP sample at 200 °C. The absorption bands at 3321.25, 1639.13, and 518.44 cm^{-1} could be assigned to stretching vibrations of the hydroxyl (−OH) group, alkene (−C═C−) group, and oxygen (O−Sn−O), respectively. Figure 5C presents the FTIR spectrum of the SNPs at 500 °C where the bands located at 3329.98, 1627.29, and 548.87 cm^{-1} correspond to hydroxyl (−OH) group stretching vibrations of phenols present in the extract; stretching vibration of alkene (−C═C−) group and oxygen/metal/oxygen (O−Sn−O) stretching vibrations, respectively. The FTIR spectrum of the SNPs obtained at 800 °C is shown in Figure 5D. The band at 592.34 cm^{-1} corresponds to the oxygen−metal−oxygen (O−Sn−O) stretching vibration group. Both samples, SNPs-2 and SNPs-5, contain stretching and bending vibrations of biomolecules on their surface, but the SNPs-8 sample does not exhibit those bonds. This suggests that annealing at higher temperatures decomposes the bio-molecules on the surface of the SNPs. Therefore, the O−Sn−O stretching vibration bands in the SNPs annealed at 200 and 800 °C increases with the increase in the annealing temperature caused by higher atomic diffusion in the crystal system that possesses size enhancement nanomaterials. Our current results resemble

https://doi.org/10.1021/acsomega.1c07099
ACS Omega 2022, 7, 15423−15438

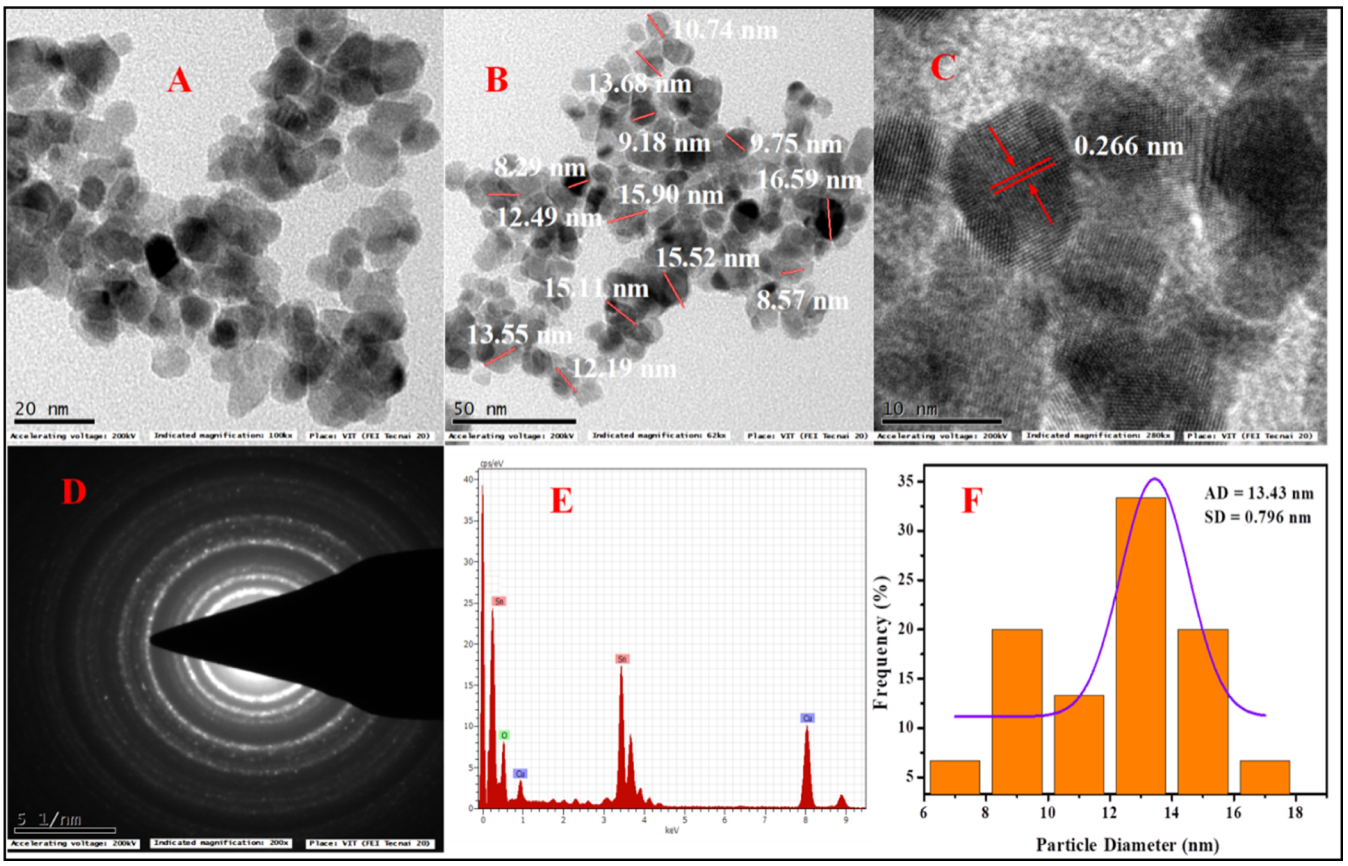

Figure 4. HR-TEM of sample SNPs-8 at annealing at 800 °C; (A) 20 nm scale magnification, (B) 50 nm scale magnification, (C) inter planar *d*-spacing, (D) SEAD pattern, (E) EDX micrograph, and (F) particle size distribution of the histogram.

recently reported results: stretching vibration of oxygen and metal, oxygen of SNPs in the range of 540−660 cm^{-1}, which indicates O−Sn−O and Sn−O stretching vibration modes reported by Paramarta et al. (2016).[38]

3.4. UV−Visible Analysis. As mentioned in the Experimental section, in the present investigation, crystalline SnO_2 nanomaterials are synthesized without using any commercial reducing or surfactant chemicals. Instead, the synthesis of the nanoparticles was performed by reducing agents that possess the cotton peel extracts that act as a capping/size controlling agent. Figure 6 represents the characteristic UV−vis absorption spectrum of the SNP samples in the band range 200−800 nm. Figure 6A−C demonstrates absorption bands at around λ_{max} = 275, 263, and 244 nm for the SNPs-2, SNPs-5, and SNPs-8, respectively. Note that the λ_{max} value shifts toward to the UV region when increasing the size of the particles. However, the maximum absorbance for sample SNPs-2 is in the visible region, and the maximum absorbance for sample SNPs-5 lies in both UV and visible regions.

In contrast, sample SNPs-8 has an absorption in the UV region. In this manner, the λ_{max} absorption value depends upon the size of the nanomaterials. With the increase in size, the maximum absorption band shifted toward the UV region. The band gap/energy gap (E_g), one of the optical properties that demonstrate the semiconducting nature of nanomaterials and the absorption coefficients for the tin oxide samples, was determined by the following II.

$$E_g = h\upsilon - [\alpha h\upsilon]^{1/2} \quad \text{(II)}$$

where E_g is the energy band gap, $h\upsilon$ is the photon energy, and α is the optical absorption coefficient. Figure 6 also shows the energy band gaps of the SNPs-2, SNPs-5, and SNPs-8 samples, obtained by extrapolating the Tauc plot $(\alpha h\upsilon)^{1/2}$ of the tin oxide nanomaterials versus the photon energy ($h\upsilon$). Note that the band gap values depend on the sintering sample. The band gap energy values are 2.68 eV (Figure 6D), 2.92 eV (Figure 6E), and 3.14 eV (Figure 6F) for the samples annealed at 200, 500, and 800 °C, respectively. Therefore, the above observation suggests that increasing the annealing process increases the band gap of the tin oxide nanomaterials. However, it has been indicated that a decrease in the band gap value is attributed to crystal defects in the material, leading to new energy levels that decrease.[39] Thus, not only the Fermi energy level but also the temperature influences the band gap of the material. The present study reveals that the material's band gap increased with the increase in sintering temperature, which might influence the decrease of crystal defects.

3.5. Surface Area and Porosity Identification by BET Analysis. BET technique was used to identify the pore diameter, specific surface area, pore volume, and size distribution of the SNP samples by possessing adsorption−desorption nitrogen isotherms. Figure 7A represents the adsorption−desorption of nitrogen isotherms of the SNPs-2 samples measured at 77 K. The BET surface area is around 153.20 m^2/g, and the pore size distribution Barrett−Joyner−Halenda (BJH) exhibits a narrow curve of calculated pore size diameter ~ 3.10 nm, as shown in Figure 7B. Similarly, the SNPs-5 sample exhibits a BET surface area ~ 90.34 m^2/g, with pore diameter 4.95 nm denoted in Figure 7C,D. In the case of the

https://doi.org/10.1021/acsomega.1c07099
ACS Omega 2022, 7, 15423−15438

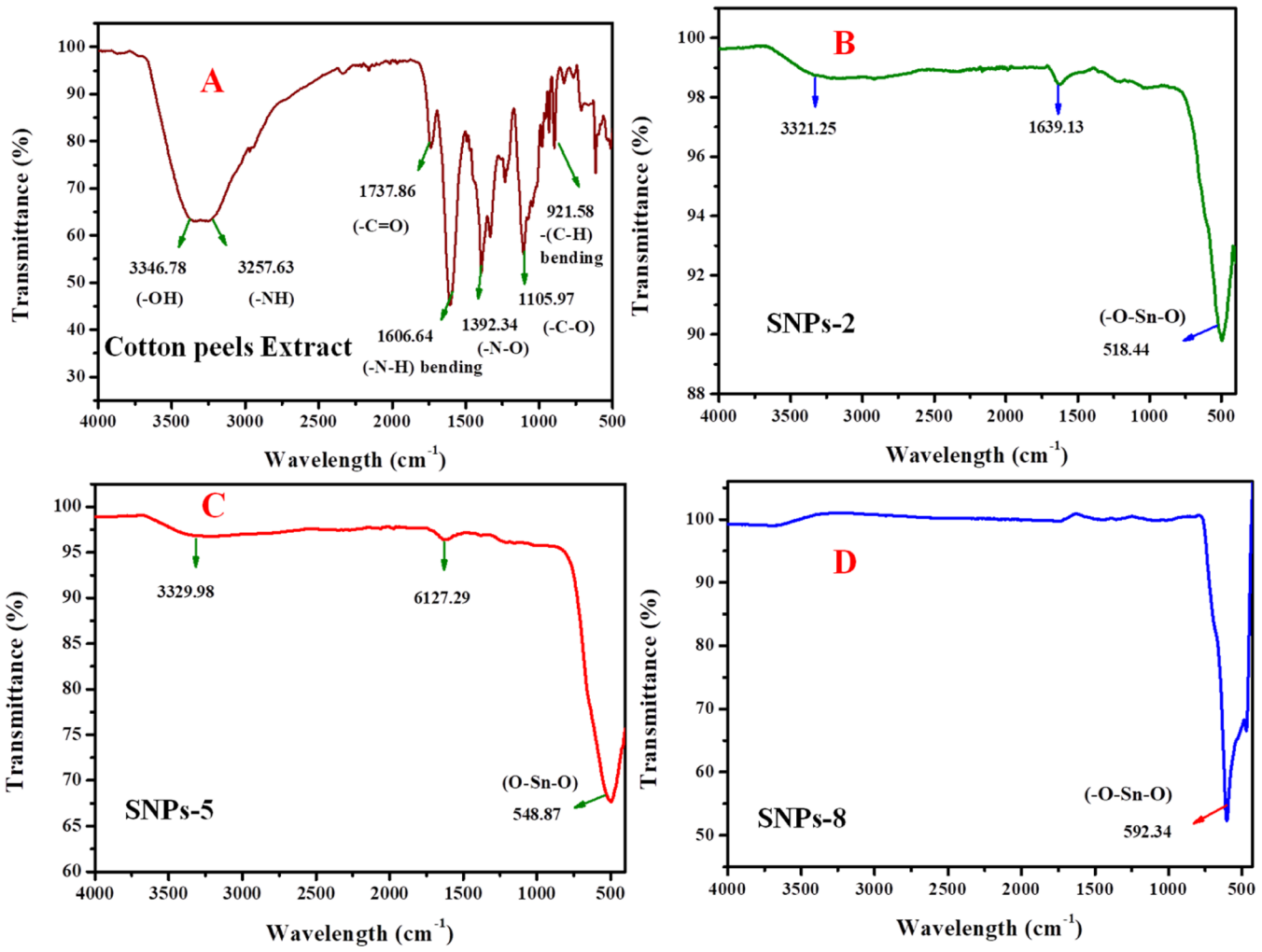

Figure 5. FT-IR analysis of cotton peel aqueous extract (A), sample SNPs-2 at 200 °C, (B), sample SNPs-5 at 500 °C (C), and sample SNPs-8 at 800 °C (D).

sample calcined at 800 °C (SNPs-8), it possesses a specific surface area ~43.72 m^2/g and pore diameter 5.41 nm, which is displayed in Figure 7E,F.

These results reveal that the sample SNPs-2 has the highest surface area compared to samples SNPs-5 and SNPs-8. From the point of view of the size and higher surface area, this material (SNPs-2) is more promising than the others to show excellent photocatalytic activity for the remediation of organic pollutants. Our results are analogous to that one reported by Ullah et al. (2017),[40] where the SNP surface area was reported to be 47.85 m^2/g for samples calcined at 600 °C and the BJH curve is narrow. However, the pore diameter was noticed to be 10.5 nm.

4. PHOTOCATALYTIC ACTIVITY FOR THE REMEDIATION OF ORGANIC POLLUTANTS

The release of excess dyes from the industry may cause environmental effects. From this point of view, nowadays, there is more and more interest in the remediation of MB and MO dyes by semiconducting materials. Thus, SNPs were tested for the photodegradation of MB and MO dyes widely used in textiles and paper. In the present work, the photocatalytic degradation of MB and MO dyes and reaction were performed under UV light exposure.

4.1. Photocatalytic Activity of SNPs for the Degradation of MB Dye. The photocatalytic activity of cotton peel extract-mediated SNPs-3, SNPs-5, and SNPs-8 nanoparticles in remediation of MB dye was carried out in the presence of UV light (λ_{max} = 254 nm) irradiation. Figure 8 shows the MB dye's absorbance spectra under regular intervals recorded in the range 200−800 nm. Strong absorption bands arise at 663 nm, representing the maximum wavelength of the MB dye, and gradually decrease intensity in the absorbance spectrum concerning time in the presence of samples SNPs-2, SNPs-5, and SNPs-8. These results are similar to those reported by Huang et al. (2018) for the degradation of MB 98.7% within 120 min using the Pd/BiOI/MnOx hollow sphere catalyst.[41] The synthesized SNP samples in the present work show a remarkable decrease of MB dye degradation in the UV−vis spectra.

The degradation was calculated using III.

$$\text{dye degradation in (\%)} = \left[\frac{C_0 - C_t}{C_0}\right] \times 100 \quad \text{(III)}$$

where C_0 is the MB concentration of absorbance and C_t is the degradation time taken for the MB absorbance. The results indicate that in the case of the SNPs-2 sample, the MB dye degradation represents 98.56% within 30 min, as shown in Figure 8A. In the case of sample SNPs-5, the MB degradation is 97.84% within 50 min, as shown in Figure 8B. However, in the case of sample SNPs-8, the degradation is 97.12% within 80 min

https://doi.org/10.1021/acsomega.1c07099
ACS Omega 2022, 7, 15423−15438

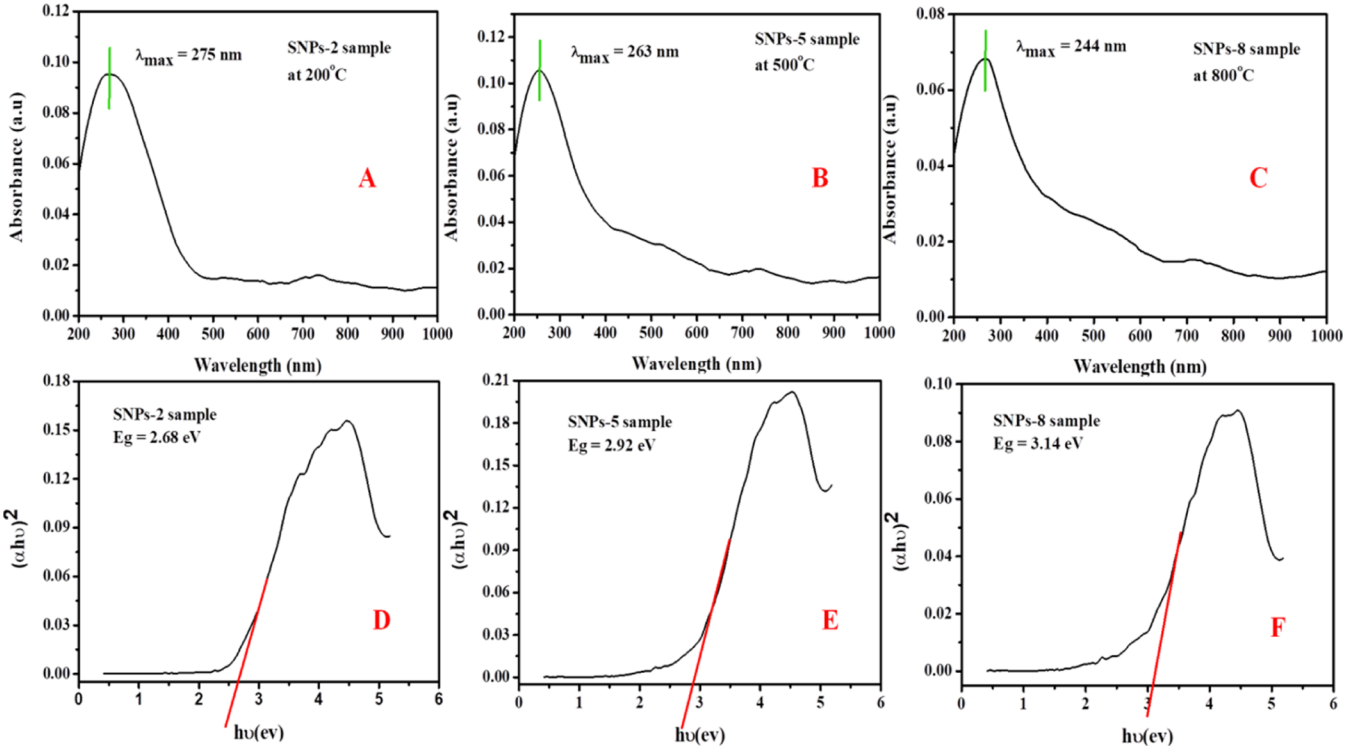

Figure 6. UV−vis absorption spectra of SNP sample at 200 °C (A), SNP sample at 500 °C (B), SNP sample at 800 °C (C), band gap energy of SNPs-2 (D), band gap energy of SNPs-5 (E), and band gap energy of SNPs-8 (F).

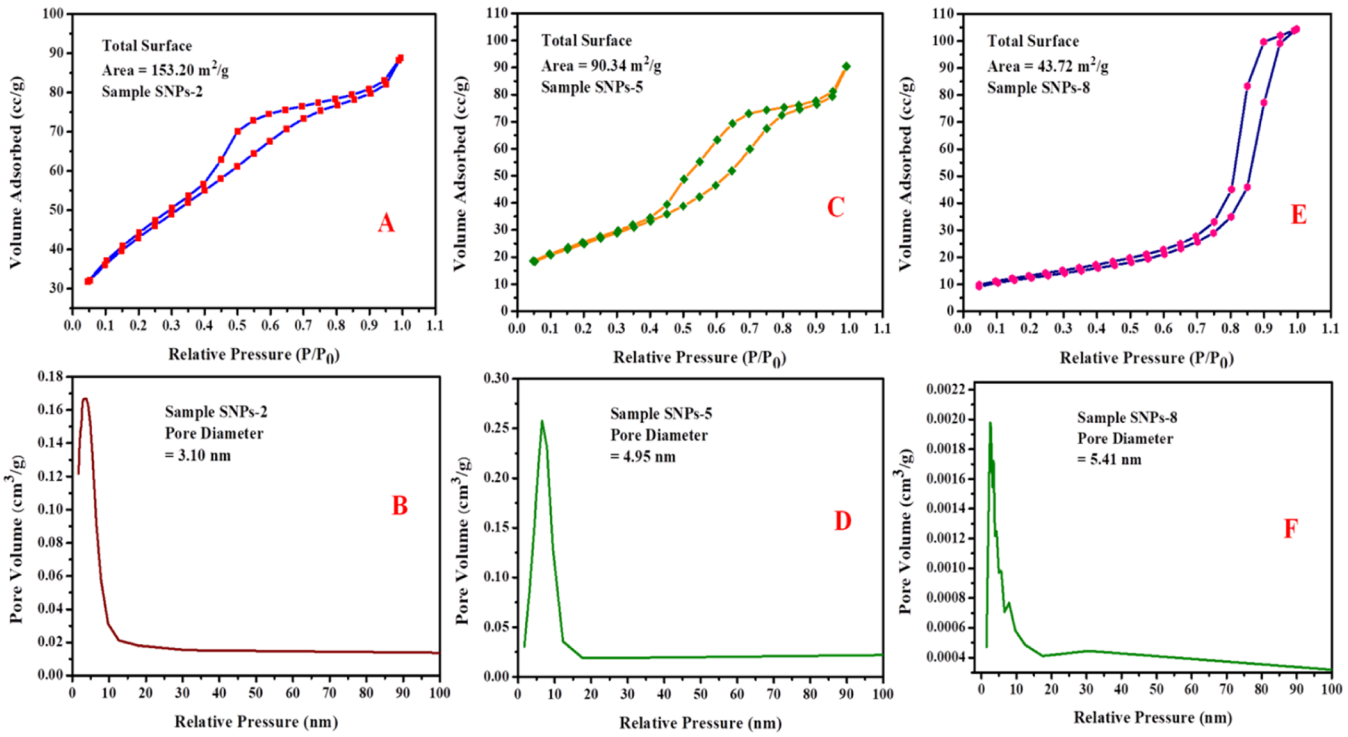

Figure 7. BET analysis of sample SNPs at 200 °C total surface area (A), pore diameter (B), at 500 °C total surface area (C), pore diameter (D), and at 800 °C total surface area (E), pore diameter (F).

in the presence of UV light, as shown in Figure 8C. The obtained degradation study is compared to other results reported in the literature in Table 2. In the beginning, the MB dye degradation was monitored without the catalyst. The results show that the degradation of MB without a catalyst for sample SNPs-2 is 9.35%, as shown in Figure 8D. In the case of sample SNPs-5, the degradation is 7.91%, as represented in Figure 8E, whereas in the case of sample SNPs-8, a 7.17% degradation occurs, as shown in Figure 8F. A previous study by Elango et al. (2016) reported that

https://doi.org/10.1021/acsomega.1c07099
ACS Omega 2022, 7, 15423−15438

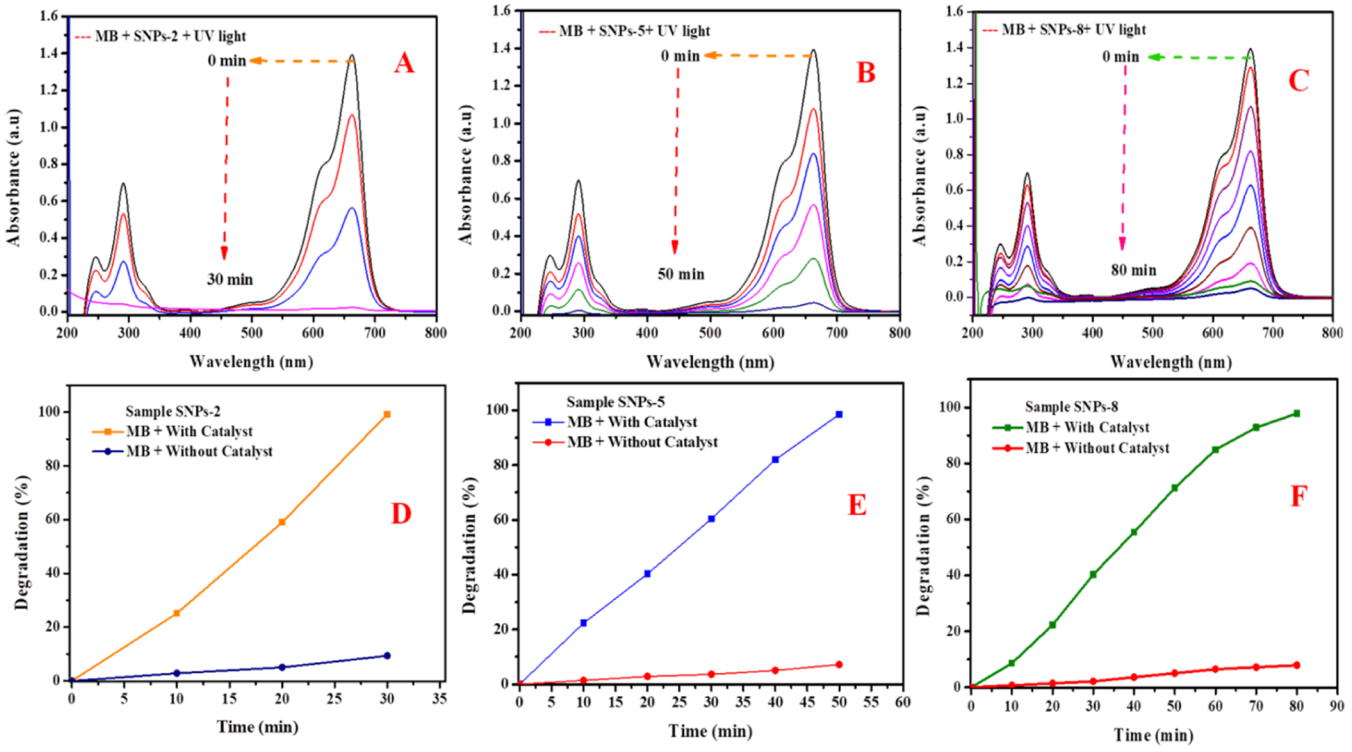

Figure 8. Photocatalytic activity of SNPs-2 for the degradation of MB dye (A), SNPs-5 for the degradation of MB dye (B), SNPs-8 for the degradation of MB dye (C), SNPs-2 percentage of MB dye degradation (D), SNPs-5 percentage of MB dye degradation (*E*), and SNPs-8 percentage of MB dye degradation (*F*).

Table 2. Comparison of Photocatalytic Activity of SNP Samples to the Degradation of MB and MO Dyes by Different Nanocatalysts

R	material used	NPs dose/dye dose	size/shape	time	degradation efficiency (%)	refs
MB	SnO_2/SnO NPs	50.00	14−70 nm/spherical shape	180 min	90.28% MB	[46]
	Sr-doped ZnO nanocatalyst	33.33	25−45 nm/hexagonal	120 min	78.50% MB	[47]
	spindle-like TiO_2	100.00	50−70 nm/spindle-like	120 min	62.70% MB	[48]
	Cu/MMT nanocatalyst	31.26	8 nm/spherical shape	120 min	95.06% MB	[49]
	SNPs-2 at 200 °C	33.33	3.97 nm/spherical shape	30 min	98.56% MB	Present Work
	SNPs-5 at 500 °C	33.33	8.48 nm/spherical shape	50 min	97.84% MB	Present Work
	SNPs-8 at 800 °C	33.33	13.43 nm/spherical shape	80 min	97.12% MB	Present Work
MO	ZnO nanocatalyst	100.00	40 nm/spherical shape	120 min	83.99% MO	[50]
	SnO_2 nanocatalyst	100.00	10−42 nm/spherical shape	120 min	94.00% MO	[51]
	$NiFe_2O_4$ nanocatalyst	50.00	34.74 nm/quasi globular-shaped	300 min	72.66% MO	[52]
	Fe nanocatalyst	12.00	7−14 nm/tetragonal shaped	100 min	95.00% MO	[53]
	SNPs-2 at 200 °C	33.33	3.97 nm/spherical shape	40 min	98.26% MO	Present Work
	SNPs-5 at 500 °C	33.33	8.48 nm/spherical shape	70 min	97.39% MO	Present Work
	SNPs-8 at 800 °C	33.33	13.43 nm/spherical shape	100 min	96.52% MO	Present Work

MB 85% degrades in 70 min of spherical shape SNPs.[42] However, there are no similar studies using SNPs.

4.2. Photocatalytic Activity for the MO Dye Degradation. The photocatalytic activity analysis was performed to evaluate the efficiency of the green synthesized SNPs in the degradation of MO under UV light irradiation. Figure 9 shows the absorbance spectra of MO dye degradation noticed between 200 and 800 nm with time intervals. The maximum absorbance occurs at $\lambda_{max} \sim 464$ nm in the UV−vis spectra. In the case of the catalyst, the degradation of MO dye in sample SNPs-2 drastically reached up to 98.26% in 40 min under UV light exposure in the UV−vis spectrum; no intermediate peaks are detected in Figure 9A. In the case of sample SNPs-5, the MO dye degradation reaches up to 97.39% within 70 min, as shown in Figure 9B, and in the case of sample SNPs-8, the degradation significantly reaches 96.52% within 100 min in the presence of UV light irradiation as represented in Figure 9C.

However, the degradation of MO dye does not change significantly without a catalyst; only 9.56% degrades under UV light irradiation, as represented in Figure 9D. Similarly, the degradation of MO in the case of sample SNPs-5 is around 8.69%, as illustrated in Figure 9E. In contrast, for sample SNPs-8, the 10.43% degradation occurs within 100 min, as shown in Figure 9F. Our results are pretty similar to those reported by Yao et al. (2021), which report MO dye degradation 91.3% after 14 h in the presence of visible light irradiation.[43] Hence, the above III determined well the % of MO dye degradation and the effectiveness of the photocatalytic treatment process. The

https://doi.org/10.1021/acsomega.1c07099
ACS Omega 2022, 7, 15423−15438

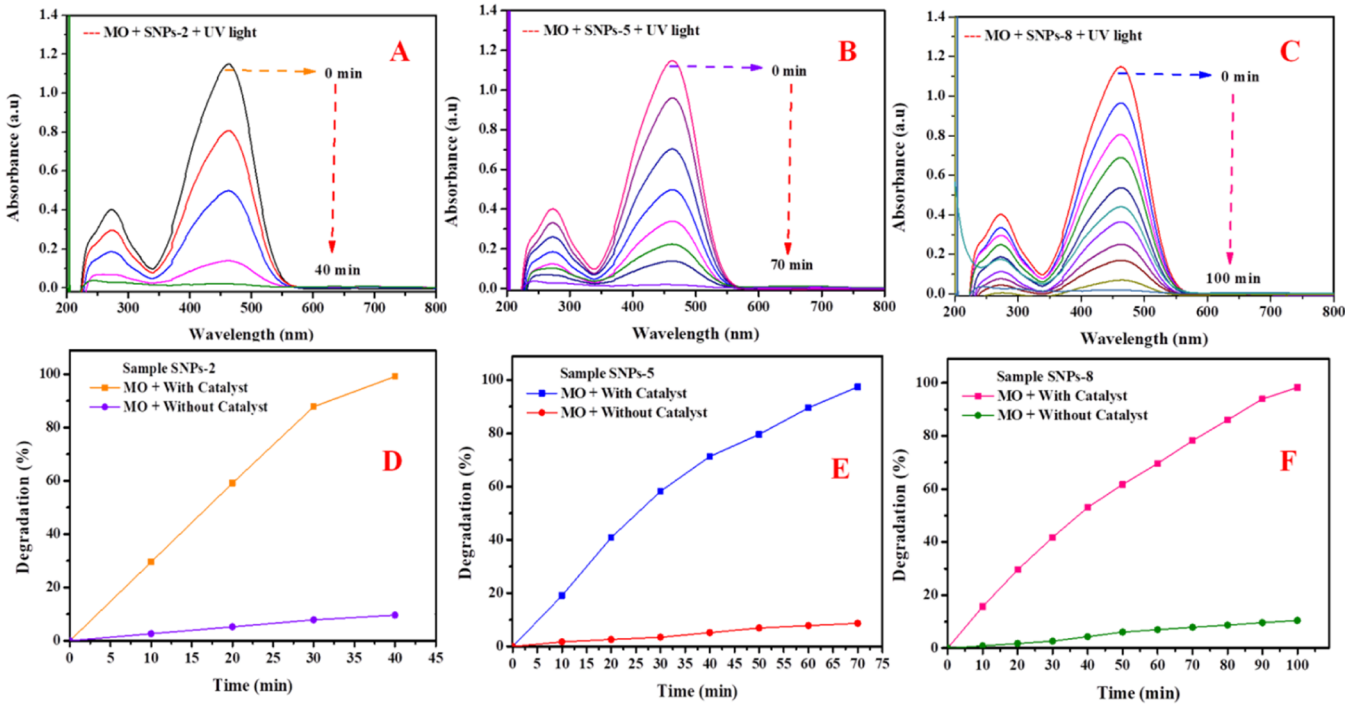

Figure 9. Photocatalytic activity of SNPs-2 for the degradation of MO dye (A), SNPs-5 for the degradation of MO dye (B), SNPs-8 for the degradation of MO dye (C), SNPs-2 percentage of MO dye degradation (D), SNPs-5 percentage of MO dye degradation (E), and SNPs-8 percentage of MO dye degradation (F).

obtained results of photodegradation of MB and MO were compared with the degradation time and the % of degradation reported literature (see Table 2).

4.3. Effect of Catalyst Dose on MO/Methyl Blue Degradation. MO/MB dye degradation was tested with 10, 20, and 30 mg catalyst sample SNPs-2 at a constant concentration of MB and MO pollutants (10 mg/L). The photodegradation efficiency of MB gradually increased from 96.42 to 99.28%, while under the same condition, the MO dye degradation efficiency increased from 96.61 to 99.15%, as indicated in Table 3. The photocatalytic of MB/MO dyes remediation was estimated from the pseudo-first-order kinetics, as follow (IV).

Table 3. Degradation (%) and with Ratio of Catalyst Dose (mg) to Dye Dose (mg) and Rate Constant of MB and MO Dye

dye name	NPs dose (mg)/dye dose (mg)	time (min)	degradation (%)	rate constant (k) min^{-1}
MB	16.66	60	96.42	0.0858
	33.33	30	98.56	0.2053
	50.00	20	99.28	0.3316
	66.66	15	99.59	0.3408
	33.33	30	98.56	0.2053
	22.22	70	97.91	0.1211
MO	16.66	70	96.61	0.1082
	33.33	40	98.26	0.2025
	50.00	30	99.15	0.3174
	66.66	20	98.48	0.3783
	33.33	40	98.26	0.2025
	22.22	80	96.96	0.1355

$$r = \mathrm{d}C = \frac{kKC}{(1 + KC)} \quad \text{(IV)}$$

where r is the MB and MO dye degradation rate, C is the concentration of MB and MO dye solution, K is the absorption coefficient of MB and MO, t is the degradation time taken for MB/MO, and k is the constant rate reaction of MB/MO. Because the initial concentration of MB/MO is C_0 = 10 mg/L, the above equation can be approximated to a pseudo-first-order model. For MB dye photodegradation, a similar procedure was previously employed to the GO/TiO_2 nanocomposite loading by Kurniawan et al. (2020).[44] The degradation of MB/MO dye by photocatalyst increased, leading to more and more active sites generated, particularly on the photocatalyst surface, increasing the number of radicals. Therefore, the amount of catalyst enormously increased the rate constant, and consequently, the degradation time was reduced for completing the reaction as noticed and represented in Table 3. The results concluded that at the high dosage catalyst improves the MO/MB dye degradation efficiency, as is represented in Figure 10A,B. However, from the results, the amount of catalyst (mg) increases the rate constant (k) and decreases the degradation duration time (t), as shown in Table 3. From the result, we concluded that the photocatalytic properties of the SNP samples exhibited against the MB and MO dye degradation. However, the degradation efficiency depends on the smaller size SNP samples (3.97, 8.48, and 13.43 nm, respectively), lower band gap energies (2.68, 2.92, and 3.14 eV, respectively), and surface area (153.20, 90.34, and 43.72 m^2/g, respectively), which play a key role in the photocatalytic dye degradation.

4.4. Effect of MO/MB Dye Concentration. The effect of MO/MB dye concentration on the degradation of MO and MB at different dye concentrations (5, 10, and 15 mg/L) is analyzed at a particular constant catalyst dose (20 mg) of photocatalyst

https://doi.org/10.1021/acsomega.1c07099
ACS Omega 2022, 7, 15423−15438

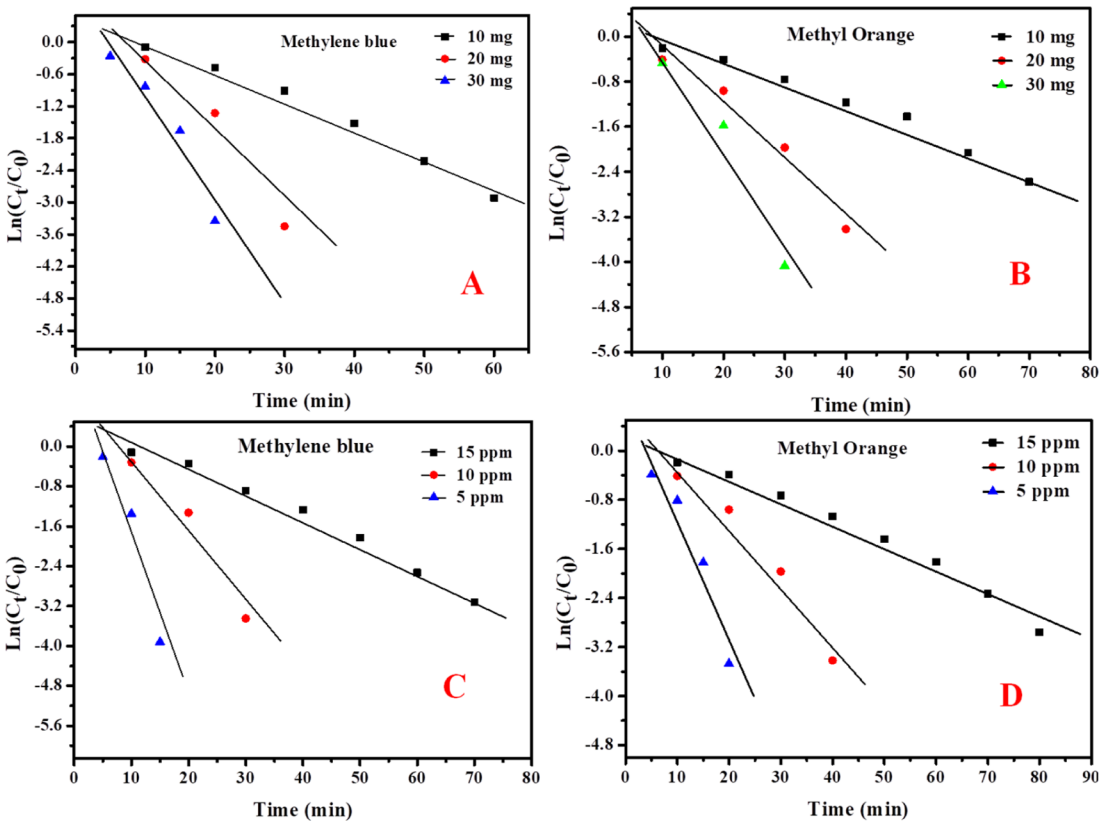

Figure 10. Kinetic plots of MB and MO dye degradation, (A) MB degradation kinetics curves for varying catalyst doses (10−30 mg), (B) MO degradation kinetics curves for varying catalyst doses (10−30 mg), (C) effect of dye concentration (5−15 mg/L) on the degradation of MB dye, and (D) effect of dye concentration (5−15 mg/L) on the degradation of MO dye.

sample SNPs-2. Figure 10C,D shows that the degradation efficiency of MB and MO dyes gradually decreased, resulting in longer degradation times. The MB and MO pollutant concentrations 5 to 15 mg/L were tested with 20 mg of SNPs-2 sample photocatalyst under UV light exposure. Table 3 shows that the MB and MO dye photodegradation rate decreased while the MB and MO dye concentration increased from 5 to 15 mg/L. However, the MB and MO dye photodegradation efficiency rate did not increase significantly. It is at a constant rate even upon increasing the concentration of the MB and MO dye solution. Similarly, Chen et al. (2017) reported the effect of dye solution concentration at a particular constant catalyst (ZnO NPs) for Congo red, MO, and DB38 dye degradation efficiency in the presence of photoirradiation.[45]

4.5. Degradation Efficiency Comparison with Published Reports. The results for the degradation efficiency of MB and MO dyes providing the corresponding ratio of SNP samples nanocatalyst dose (mg) to dye concentration (mg/mg), size, surface area, shape, band gap energy of the NPs, degradation efficiency, and time (min) are listed in Table 2. Our results are compared to similar reported works, including the photocatalyst SnO/SnO_2 hybrids, spindle-like TiO_2 nanocatalysts, Sr-doped ZnO nanocatalysts, as well as copper nanoparticles supported with montmorillonite clays nanocatalyzed for the degradation efficiency of MB dye.[46−49] Moreover, ZnO nanocatalysts, SnO_2 nanocatalysts, and Fe nanocatalyst degradation of MO dye reported in references 50−53 and degradation efficiencies are compared in the table.

It is noticed that the degradation time depends on the ratio of the SNP photocatalyst dose to dye concentration (mg/mg), shape, surface area, and particle size of the NPs, as represented in Table 2. However, there have been recent studies that report that during the degradation of MB and MO by nano photocatalysts, massive free radicals that represent ROS are released, reacting with the dye molecules and leading to nontoxic products such as mineral acids, water molecules (H_2O), and carbon dioxide (CO_2), which support our observation. Thus, the synthesized SNP samples exhibit extremely enhanced degradation efficiency summarized to the recently reported literature given in Table 2. However, it strongly depends on the smaller particle size and uniform spherical shape of the nanoparticles. The MB degradation 98.56 percentage degraded within 30 min for a rate constant (k) 0.2053 min^{-1}, similar to MO 98.26 percentage degradation within 40 min concerning rate constant (k) 0.2025 min^{-1}. However, the SNP sample photocatalyst dye degradation reaction experiment was processed at a particular constant (20 mg) photocatalyst and 60 mL of volume of dye solution at a specific dye concentration (10 mg/L) under UV light exposure. Similar experimental studies of the effect of photocatalytic at varied catalyst doses and concentrations of dye solution and that provide results of rate constant (k), degradation efficiency, and degradation time are tabulated in Table 2. Therefore, the synthesized SNP samples exhibited extraordinary photocatalytic activity performance and could be promising materials utilized in degradation water purification and toxic and hazardous organic pollutant dyes.

4.6. Possible Mechanism of MB and MO Dye Degradation. The reasonable possible mechanism of MB and MO dye degradation demonstrated by the obtained

https://doi.org/10.1021/acsomega.1c07099
ACS Omega 2022, 7, 15423−15438

semiconductor SnO_2 nanomaterials in the present work is represented in Scheme 1. Photocatalyst semiconductors have

Scheme 1. Possible Mechanism of MB and MO Dye Degradation by SNPs Obtained in This Work

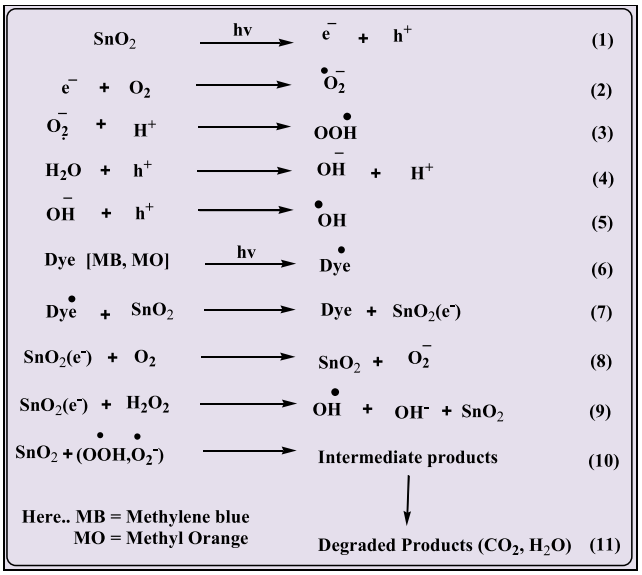

many characteristics and properties (such as small size, high surface area, low band gap energy, tetragonal structure, and so forth), which can influence the removal of MB and MO dyes. For example, the tetragonal structure of tin oxide nanomaterials has shown high photocatalytic activity and feasibility in dye removal.[54] The photocatalytic activity described in Scheme 1 is carried out in two steps. The first step includes the absorbance of dye molecules on the surface of the SNP sample during the constant stirring process without UV light exposure. The second step consists of forming electron−hole pairs, which generates superoxide radicals and hydroxide radicals in the SNP matrix, which degrade the dye molecules to complete mineralization (H_2O and CO_2) of the pollutant molecules.

The feasible mechanism describes the various reaction succession steps occurring during the degradation of MB and MO dyes in the presence of SnO_2 nanomaterials under UV light irradiation and assumes the excess of highly ROS in the solution. Vidya et al. (2017) proposed a similar mechanism for the ZnO NP photocatalytic activity of Cong red dye degradation in the presence of UV light exposure.[55] The possible mechanism involves sequence steps described by the following equations. UV light bombarding the SNP nanomaterials generates electrons and transfers electrons from the valence band to the conduction band with corresponding energy higher than the band gap energy of the SNP nanomaterials that should promote holes in the valence band and generate electrons in the conduction band. This process might generate high ROS species that are reactive with MB and MO dye molecules such as successive carbon dioxide and water molecules. At the beginning, under UV light irradiation, electrons moved from the valence band to the conduction band on the surface of the SNPs, which is represented in eq 1. In this way, conduction band electrons (e_{CB}^-) readily react with oxygen to generate superoxide ($O_2^{-\bullet}$) ions, as shown in eq 2, and subsequently, these highly reactive oxide ions react with hydrogen (H^+) ions to release the −OOH, as represented in eq 3, whereas in the valence band, (hv_{VB}^+) holes readily contact with water molecules to produce hydroxide ($-OH^-$) ions which in turn generate highly active hydroxide radicals ($-^{\bullet}OH$), as represented in eqs 4 and 5. The produced −OOH can readily react with conduction-band electrons and hydrogen ions to produce highly active superoxide (H_2O_2) molecules. Eventually, the cleavage of hydrogen peroxide (H_2O_2) molecules occurs to produce the highly active hydroxyl radical ($-^{\bullet}OH$), and also, the photo-electrons diminish the oxygen molecules (O_2) adsorbed on the SNP catalyst surface generating superoxide ($O_2^{-\bullet}$) radicals. Eventually, MB and MO dye molecules are decomposed by the formed highly active hydroxyl ($^{\bullet}OH$) radicals and superoxide ($O_2^{-\bullet}$) radicals to produce mineral acids, H_2O, and CO_2, as shown in eqs 6−11. This mechanism is similar to that proposed by Zangeneh et al., (2015), which assumes the formation of radicals during dyes' degradation.[56]

Liu et al., (2021) reported charge-carrier trapping on the surface of the materials based on the band gap energy. The higher level of energy than the band gap of the materials leads to electron transfer from the conduction band to the valence band and generating hydroxide and superoxide radical's degradation of the dye molecules.[57] The photocatalytic reactions take place provided that the semiconductor receives irradiation photons with energy greater than the band gap. An irradiating photon with insufficient energy leads to the failure of electron transition and then degradation is not possible to carbon dioxide and water molecules. Li et al. (2021) reported reactive species scavenging experiments and electron spin resonance which revealed that hydroxyl radicals ($^{\bullet}OH$), superoxide radical anions ($O_2^{-\bullet}$), and photogenerated holes (h^+) played critical roles for the photocatalytic degradation.[58]

Recent reports discussed the effect of the pH for the degradation of MB and MO dyes. Alkaykh et al. (2020) reported the effect of pH for the MB dye degradation, where at pH2, it shows the 15% removal of MB dyes; however, at pH 9, it shows 60% MB dye removal.[59] Wu et al. (2022) studied the effect of pH from 4 to 9 for the methylene dye degradation that possesses under acidic condition pH 4 is 63.88% degradation of the MB dye; however, at pH 9 basic condition, it shows 60.73% degradation, but at pH 6 neutral condition, it shows the 95.94% degradation of MB dye removal.[60] Abbasi and Hasanpour, (2017) studied the effect of pH from 4 to 10 that shows at pH 7 its higher efficiency of 99% MO dye removal than at pH 4 and pH 10.[61] Cai et al. (2017) studied the effect of pH at 3−9 that represents that at pH 3 and 5, it shows the higher decolorization efficiency of MO at 99 and 98%; however, at pH 9 alkaline medium, it shows 88% of MO decolorization efficiency.[62] Adeel et al. (2021) studied the effect of pH at 2−10; however, at pH 4 and 2, the highest photodegradation of MO rate constant was reported, that is, 0.0144 and 0.0099 min^{-1}, but in the case of at pH 10, 0.0043 min^{-1} degradation efficiency was reported.[63]

4.7. Reusability of the SNP Sample. The reusability stability of the synthesized photocatalyst sample SNPs-2 has been studied. The SNPs-2 sample residue was collected after the degradation of MB and MO under UV-light exposure, centrifugated, washed, and then reused five consecutive cycles under identical conditions. The removal of MB and MO using the SNPs-2 sample offer after the first^t cycle the highest photodegradation 98.56% for MB and 98.26% for MO. After that, the second cycle removal for MB and MO was 97.84 and 96.52%, respectively. In the case of the third cycle, the MB and MO degradations were 97.12 and 95.65%, respectively. In the case of the fourth cycle, the MB and MO degradation reached 96.54 and 93.91%, respectively. Eventually, in the fifth cycle, the

https://doi.org/10.1021/acsomega.1c07099
ACS Omega 2022, 7, 15423−15438

photocatalytic activity gradually decreased to 95.82% for MB and 92.17% for MO. The degradation versus cycle plot is shown in Figure 11A. Thus, sample SNPs-2 exhibits excellent

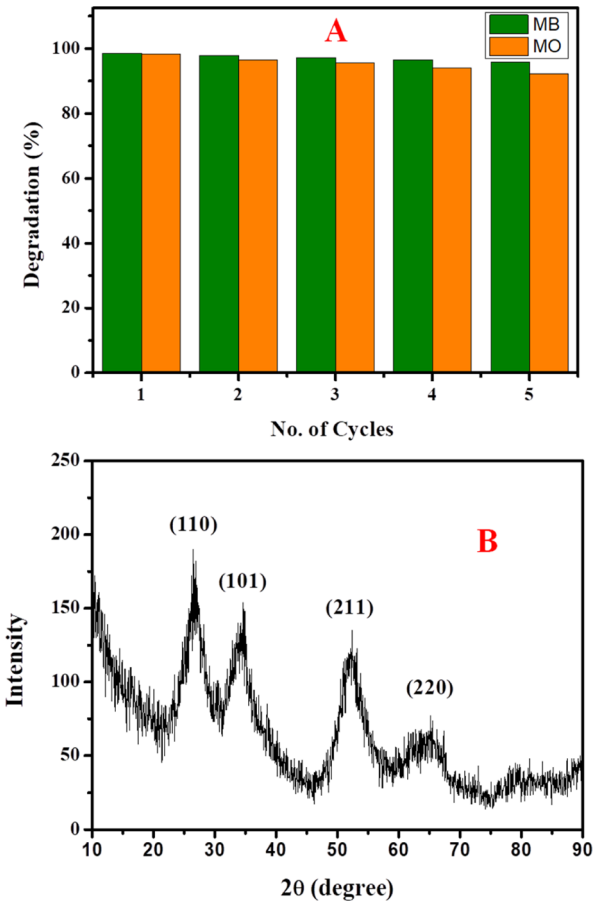

Figure 11. Recyclability check of biosynthesized sample SNPs-3 for the degradation of MB and MO under identical experimental conditions (A) and XRD pattern after five consecutive cycles for sample SNPs-3 (B).

reusability for the photodegradation of MB and MO pollutant dyes. Moreover, to authenticate the stability of sample SNPs-2 after five cycles, any phase change was analyzed by powder XRD (see Figure 11B). Based on the results, the crystallization of the recovered catalyst remains unchanged even after five cycles of use when compared to the as synthesized SNPs-2 sample. Therefore, we concluded that the synthesized SNPs-2 sample is stable and maintains its outstanding photocatalytic activity for consecutive cycles.

5. CONCLUSIONS

The present study carried out a simple, nontoxic, eco-friendly, and cost-effective method to produce SNP nanomaterials through the agro-waste cotton boll peel aqueous extract. SNPs were successfully synthesized at different temperatures of 200, 500, and 800 °C without involving toxic chemicals or solvents. XRD patterns confirmed that the crystal structure is tetragonal, and the average crystallite sizes for the SNP samples obtained after 200, 500, and 800 °C are 4.72, 9.68, and 14.06 nm, respectively. HR-TEM images manifested spherical shaped samples with sizes 3.79, 8.48, and 13.43 nm for SNP-2, SNP-5, and SNP-8, respectively. The samples were further analyzed by FT-IR, UV−vis spectroscopy, and BET analysis, and their photocatalytic activity for the degradation of MB and MO was inspected. From the result, we concluded that the smaller size of the SNPs-2 sample (3.79 nm), the lower band gap energy (2.68 eV) and higher the surface area (153.20 m^2/g) exhibited superior performance of photocatalytic efficiency for the degradation of MB/MO. Therefore, MB dye 98.56% degradation within 30 min and MO dye 98.26% degradation within 40 min, respectively, under UV light exposure. Moreover, we have also studied the effect of catalyst and the effect of dye concentration. As the amount of catalyst (10 mg to 30 mg) increases, the rate constant increases and decreases the degradation duration time. However, when the dye concentration (5−15 mg/L) increases, the rate constant decreases, and the degradation duration time increases. Consequently, the synthesized SNP samples are promising materials to be used as a photocatalyst for the remediation of pollutant dyes.

AUTHOR INFORMATION

Corresponding Authors

Luis De Los Santos Valladares − *Laboratorio de Cerámicos y Nanomateriales, Facultad de Ciencias Físicas, Universidad Nacional Mayor de San Marcos, Lima 14, Peru; Cavendish Laboratory, Department of Physics, University of Cambridge, Cambridge CB3 OHE, U.K.; School of Materials Science and Engineering, Northeastern University, Shenyang 110819 Liaoning, People's Republic of China;* orcid.org/0000-0001-5930-9916; Email: ld301@cam.ac.uk

Pratap Kollu − *CASEST, School of Physics, University of Hyderabad, Hyderabad 500046 Telangana, India;* orcid.org/0000-0001-6250-9396; Email: pratapk@uohyd.ac.in

Authors

Boya Palajonnala Narasaiah − *CASEST, School of Physics, University of Hyderabad, Hyderabad 500046 Telangana, India; Laboratorio de Cerámicos y Nanomateriales, Facultad de Ciencias Físicas, Universidad Nacional Mayor de San Marcos, Lima 14, Peru*

Pravallika Banoth − *CASEST, School of Physics, University of Hyderabad, Hyderabad 500046 Telangana, India*

Arya Sohan − *CASEST, School of Physics, University of Hyderabad, Hyderabad 500046 Telangana, India*

Badal Kumar Mandal − *Department of Chemistry, School of Advanced Sciences, Vellore Institute of Technology, Vellore 632014 Tamil Nadu, India*

Angel G. Bustamante Dominguez − *Laboratorio de Cerámicos y Nanomateriales, Facultad de Ciencias Físicas, Universidad Nacional Mayor de San Marcos, Lima 14, Peru*

Complete contact information is available at: https://pubs.acs.org/10.1021/acsomega.1c07099

Author Contributions

#B.P.N. and P.B. are equally contributing first authors.

Notes

The authors declare no competing financial interest.

ACKNOWLEDGMENTS

This work was supported by the "Incorporation de Investigadores program" CONCYTEC—FONDECYT. UNMSM (contrat no. 12-2019-FONDECYT-BM-INC.INV.). P.K., P.B., and A.S. thank the Institute of Eminence (IoE), Ministry of

https://doi.org/10.1021/acsomega.1c07099
ACS Omega 2022, 7, 15423−15438

Human Resource Development (MHRD), Grant number: UoH-IoE-RC2-21-017 at University of Hyderabad, India.

REFERENCES

(1) Mourdikoudis, S.; Kostopoulou, A.; LaGrow, A. P. Magnetic Nanoparticle Composites: Synergistic Effects and Applications. *Adv. Sci.* **2021**, *8*, 2004951.
(2) Singh, J.; Dutta, T.; Kim, K. H.; Rawat, M.; Samddar, P.; Kumar, P. Green synthesis of metals and their oxide nanoparticles: applications for environmental remediation. *J. Nanobiotechnol.* **2018**, *16*, 84.
(3) Iravani, S. Green synthesis of metal nanoparticles using plants. *Green Chem.* **2011**, *13*, 2638−2650.
(4) Shamaila, S.; Sajjad, A. K. L.; Ryma, N.-u. -A.; Farooqi, S. A.; Jabeen, N.; Majeed, S.; Farooq, I. Advancements in nanoparticle fabrication by hazard free eco-friendly green routes. *Appl. Mater. Today* **2016**, *5*, 150−199.
(5) Kumar, K. M.; Mandal, B. K.; Tammina, S. K. Green synthesis of nano platinum using naturally occurring polyphenols. *RSC Adv.* **2013**, *3*, 4033−4039.
(6) Mazari, S. A.; Ali, E.; Abro, R.; Khan, F. S. A.; Ahmed, I.; Ahmed, M.; Nizamuddin, S.; Siddiqui, T. H.; Hossain, N.; Mubarak, N. M.; Shah, A. Nanomaterials: Applications, waste-handling, environmental toxicities, and future challenges - A review. *J. Environ. Chem. Eng.* **2021**, *9*, 105028.
(7) Palanisamy, G.; Bhuvaneswari, K.; Srinivasan, M.; Vignesh, S.; Elavarasan, N.; Venkatesh, G.; Pazhanivel, T.; Ramasamy, P. Two-dimensional g-C3N4 nanosheets supporting Co3O4-V2O5 nanocomposite for remarkable photodegradation of mixed organic dyes based on a dual Z-scheme photocatalytic system. *Diamond Relat. Mater.* **2021**, *118*, 108540.
(8) Choi, E.; Lee, D.; Shin, H. J.; Kim, N.; Valladares, L. D. L. S.; Seo, J. Role of oxygen vacancy sites on the temperature-dependent photoluminescence of SnO_2 nanowires. *J. Phys. Chem. C* **2021**, *125*, 14974−14978.
(9) Suthakaran, S.; Dhanapandian, S.; Krishnakumar, N.; Ponpandian, N. Hydrothermal synthesis of SnO_2 nanoparticles and its photocatalytic degradation of methyl violet and electrochemical performance. *Mater. Res. Express* **2019**, *6*, 0850i3.
(10) Nejati-Moghadam, L.; Esmaeili, B. K. A.; Salavati, N. M.; Safardoust, H. Synthesis and characterisation of SnO_2 nanostructures prepared by a facile precipitation method. *J. Nanostruct.* **2015**, *5*, 47−53.
(11) Zhang, L.; Ren, X.; Luo, Y.; Shi, X.; Asiri, A. M.; Li, T.; Sun, X. Ambient NH_3 synthesis *via* electrochemical reduction of N_2 over cubic sub-micron SnO_2 particles. *Chem. Commun.* **2018**, *54*, 12966−12969.
(12) Haspulat, B.; Sarıbel, M.; Kamış, H. Surfactant assisted hydrothermal synthesis of SnO nanoparticles with enhanced photocatalytic activity. *Arab. J. Chem.* **2020**, *13*, 96−108.
(13) Maharajan, S.; Kwon, N. H.; Brodard, P.; Fromm, K. M. A Nano-Rattle SnO2@carbon Composite Anode Material for High-Energy Li-ion Batteries by Melt Diffusion Impregnation. *Nanomaterials* **2020**, *10*, 804.
(14) Karmaoui, M.; Jorge, A. B.; McMillan, P. F.; Aliev, A. E.; Pullar, R. C.; Labrincha, J. A.; Tobaldi, D. M. One-Step Synthesis, Structure, and Band Gap Properties of SnO2 Nanoparticles Made by a Low Temperature Nonaqueous Sol-Gel Technique. *ACS Omega* **2018**, *3*, 13227−13238.
(15) Zhu, K.; Lv, Y.; Liu, J.; Wang, W.; Wang, C.; Li, S.; Wang, P.; Zhang, M.; Meng, A.; Li, Z. Facile fabrication of g-C3N4/SnO2 composites and ball milling treatment for enhanced photocatalytic performance. *J. Alloys Compd.* **2019**, *802*, 13−18.
(16) Chavali, M. S.; Nikolova, M. P. Metal oxide nanoparticles and their applications in nanotechnology. *SN Appl. Sci.* **2019**, *1*, 607.
(17) Yuliarto, B.; Septiani, N. L. W.; Kaneti, Y. V.; Iqbal, M.; Gumilar, G.; Kim, M.; Na, J.; Wu, K. C.-W.; Yamauchi, Y. Green synthesis of metal oxide nanostructures using naturally occurring compounds for energy, environmental, and bio-related applications. *New J. Chem.* **2019**, *43*, 15846−15856.
(18) Diallo, A.; Manikandan, E.; Rajendran, V.; Maaza, M. Physical & enhanced photocatalytic properties of green synthesized SnO2 nanoparticles via Aspalathus linearis. *J. Alloys Compd.* **2016**, *681*, 561−570.
(19) Matussin, S.; Harunsani, M. H.; Tan, A. L.; Khan, M. M. Plant-Extract-Mediated SnO2 Nanoparticles: Synthesis and Applications. *ACS Sustain. Chem. Eng.* **2020**, *8*, 3040−3054.
(20) Singh, J.; Kaur, H.; Kukkar, D.; Mukamia, V. K.; Kumar, S.; Rawat, M. Green synthesis of SnO2 NPs for solar light induced photocatalytic applications. *Mater. Res. Express* **2019**, *6*, 115007.
(21) Bhattacharjee, A.; Ahmaruzzaman, M. A novel and green process for the production of tin oxide quantum dots and its application as a photocatalyst for the degradation of dyes from aqueous phase. *J. Colloid Interface Sci.* **2015**, *448*, 130−139.
(22) Sinha, T.; Ahmaruzzaman, M.; Adhikari, P. P.; Bora, R. Green and Environmentally Sustainable Fabrication of Ag-SnO2 Nanocomposite and Its Multifunctional Efficacy As Photocatalyst and Antibacterial and Antioxidant Agent. *ACS Sustain. Chem. Eng.* **2017**, *5*, 4645−4655.
(23) Sudhaparimala, S.; Vaishnavi, M. Biological synthesis of nano composite SnO2- ZnO - Screening for efficient photocatalytic degradation and antimicrobial activity. *Mater. Today Proc.* **2016**, *3*, 2373−2380.
(24) Li, A. J.; Pal, V. K.; Kannan, K. A review of environmental occurrence, toxicity, biotransformation and biomonitoring of volatile organic compounds. *Environ. Chem. Ecotoxicol.* **2021**, *3*, 91−116.
(25) Rueda-Marquez, J. J.; Levchuk, I.; Fernández Ibañez, P.; Sillanpää, M. A critical review on application of photocatalysis for toxicity reduction of real wastewaters. *J. Clean. Prod.* **2020**, *258*, 120694.
(26) Li, Y.; Chang, H.; Yan, H.; Tian, S.; Jessop, P. G. Reversible Absorption of Volatile Organic Compounds by Switchable-Hydrophilicity Solvents: A Case Study of Toluene with N,N-Dimethylcyclohexylamine. *ACS Omega* **2020**, *6*, 253−264.
(27) Li, Y.; Liu, K.; Zhang, J.; Yang, J.; Huang, Y.; Tong, Y. Engineering the Band-Edge of Fe2O3/ZnO Nanoplates via Separate Dual Cation Incorporation for Efficient Photocatalytic Performance. *Ind. Eng. Chem. Res.* **2020**, *59*, 18865−18872.
(28) Li, D.; Song, H.; Meng, X.; Shen, T.; Sun, J.; Han, W.; Wang, X. Effects of Particle Size on the Structure and Photocatalytic Performance by Alkali-Treated TiO2. *Nanomaterials* **2020**, *10*, 546.
(29) Tuan, P. V.; Hieu, L. T.; Tan, V. T.; Phuong, T. T.; Tran Thi Quỳnh, H.; Khiem, T. N. The dependence of morphology, structure, and photocatalytic activity of SnO2/rGO nanocomposites on hydrothermal temperature. *Mater. Res. Express* **2019**, *6*, 106204.
(30) Jiang, Y.; Zhao, H.; Liang, J.; Yue, L.; Li, T.; Luo, Y.; Liu, Q.; Lu, S.; Asiri, A. M.; Gong, Z.; Sun, X. Anodic oxidation for the degradation of organic pollutants: anode materials, operating conditions and mechanisms. A mini review. *Electrochem. Commun.* **2021**, *123*, 106912.
(31) Li, Y.; Yang, Q.; Wang, Z.; Wang, G.; Zhang, B.; Zhang, Q.; Yang, D. Rapid fabrication of SnO2 nanoparticle photocatalyst: computational understanding and photocatalytic degradation of organic dye. *Inorg. Chem. Front.* **2018**, *5*, 3005−3014.
(32) Huang, Y.; Li, K.; Lin, Y.; Tong, Y.; Liu, H. Enhanced Efficiency of Electron-Hole Separation in Bi2 O2 CO3 for Photocatalysis via Acid Treatment. *ChemCatChem* **2018**, *10*, 1982−1987.
(33) Huang, Y.; Lu, Y.; Lin, Y.; Mao, Y.; Ouyang, G.; Liu, H.; Zhang, S.; Tong, Y. Cerium-based hybrid nanorods for synergetic photothermocatalytic degradation of organic pollutants. *J. Mater. Chem. A* **2018**, *6*, 24740−24747.
(34) Siripireddy, B.; Mandal, B. K. Facile green synthesis of zinc oxide nanoparticles by Eucalyptus globulus and their photocatalytic and antioxidant activity. *Adv. Powder Technol.* **2017**, *28*, 785−797.
(35) Osuntokun, J.; Onwudiwe, D. C.; Ebenso, E. E. Biosynthesis and Photocatalytic Properties of SnO2 Nanoparticles Prepared Using Aqueous Extract of Cauliflower. *J. Cluster Sci.* **2017**, *28*, 1883−1896.
(36) Ma, C. M.; Hong, G. B.; Lee, S. C. Facile Synthesis of Tin Dioxide Nanoparticles for Photocatalytic Degradation of Congo Red Dye in Aqueous Solution. *Catalysts* **2020**, *10*, 792.

https://doi.org/10.1021/acsomega.1c07099
ACS Omega 2022, 7, 15423−15438

(37) Arumugam, M.; Manikandan, D. B.; Dhandapani, E.; Sridhar, A.; Balakrishnan, K.; Markandan, M.; Ramasamy, T. Green synthesis of zinc oxide nanoparticles (ZnO NPs) using Syzygium cumini: Potential multifaceted applications on antioxidants, cytotoxic and as nano-nutrient for the growth of Sesamum indicum. *Environ. Technol. Innovation* **2021**, *23*, 101653.
(38) Paramarta, V.; Taufik, A.; Saleh, R. Better adsorption capacity of SnO2 nanoparticles with different graphene addition. *J. Phys.: Conf. Ser.* **2016**, *776*, 012039.
(39) Haq, S.; Rehman, W.; Waseem, M.; Javed, R.; Mahfooz-ur-Rehman, M.; Shahid, M. Effect of heating on the structural and optical properties of TiO2 nanoparticles: antibacterial activity. *Appl. Nanosci.* **2018**, *8*, 11−18.
(40) Ullah, H.; Khan, I.; Yamani, Z. H.; Qurashi, A. Sonochemical-driven ultrafast facile synthesis of SnO2 nanoparticles: Growth mechanism structural electrical and hydrogen gas sensing properties. *Ultrason. Sonochem.* **2017**, *34*, 484−490.
(41) Huang, Y.; Xu, H.; Yang, H.; Lin, Y.; Liu, H.; Tong, Y. Efficient charges separation using advanced BiOI-based hollow spheres decorated with palladium and manganese dioxide nanoparticles. *ACS Sustainable Chem. Eng.* **2018**, *6*, 2751−2757.
(42) Elango, G.; Roopan, S. M. Efficacy of SnO 2 nanoparticles toward photocatalytic degradation of methylene blue dye. *J. Photochem. Photobiol., B* **2016**, *155*, 34−38.
(43) Yao, X.; Zhang, B.; Cui, S.; Yang, S.; Tang, X. Fabrication of SnSO4-modified TiO2 for enhance degradation performance of methyl orange (MO) and antibacterial activity. *Appl. Surf. Sci.* **2021**, *551*, 149419.
(44) Kurniawan, T. A.; Mengting, Z.; Fu, D.; Yeap, S. K.; Othman, M. H. D.; Avtar, R.; Ouyang, T. Functionalizing TiO2 with graphene oxide for enhancing photocatalytic degradation of methylene blue (MB) in contaminated wastewater. *J. Environ. Manage.* **2020**, *270*, 110871.
(45) Chen, X.; Wu, Z.; Liu, D.; Gao, Z. Preparation of ZnO photocatalyst for the efficient and rapid photocatalytic degradation of azo dyes. *Nanoscale Res. Lett.* **2017**, *12*, 143.
(46) Santhi, K.; Rani, C.; Karuppuchamy, S. Synthesis and characterisation of a novel SnO/SnO_2 hybrid photocatalyst. *J. Alloys Compd.* **2016**, *662*, 102−107.
(47) Yousefi, R.; Jamali-Sheini, F.; Cheraghizade, M.; Khosravi-Gandomani, S.; Sáaedi, A.; Huang, N. M.; Basirun, W. J.; Azarang, M. Enhanced visible-light photocatalytic activity of strontium-doped zinc oxide nanoparticles. *Mater. Sci. Semicond. Process.* **2015**, *32*, 152−159.
(48) Arunkumar, S.; Alagiri, M. Synthesis and Characterization of Spindle-Like TiO2 Nanostructures and Photocatalytic Activity on Methyl Orange and Methyl Blue Dyes Under Sunlight Radiation. *J. Cluster Sci.* **2017**, *28*, 2635−2643.
(49) Mekewi, M. A.; Darwish, A. S.; Amin, M. S.; Eshaq, G.; Bourazan, H. A. Copper nanoparticles supported onto montmorillonite clays as efficient catalyst for methylene blue dye degradation. *Egypt. J. Pet.* **2016**, *25*, 269−279.
(50) Karnan, T.; Selvakumar, S. A. S. Biosynthesis of ZnO nanoparticles using rambutan (Nephelium lappaceumL.) peel extract and their photocatalytic activity on methyl orange dye. *J. Mol. Struct.* **2016**, *1125*, 358−365.
(51) Srivastava, N.; Mukhopadhyay, M. Biosynthesis of SnO2 Nanoparticles Using Bacterium Erwinia herbicola and Their Photocatalytic Activity for Degradation of Dyes. *Ind. Eng. Chem. Res.* **2014**, *53*, 13971−13979.
(52) Hirthna; Sendhilnathan, S.; Rajan, P. I.; Adinaveen, T. Synthesis and Characterization of $NiFe_2O_4$ Nanoparticles for the Enhancement of Direct Sunlight Photocatalytic Degradation of Methyl Orange. *J. Supercond. Novel Magn.* **2018**, *31*, 3315−3322.
(53) Radini, I. A.; Hasan, N.; Malik, M. A.; Khan, Z. Biosynthesis of iron nanoparticles using Trigonella foenum-graecum seed extract for photocatalytic methyl orange dye degradation and antibacterial applications. *J. Photochem. Photobiol., B* **2018**, *183*, 154−163.
(54) Najjar, M.; Hosseini, H. A.; Masoudi, A.; Sabouri, Z.; Mostafapour, A.; Khatami, M.; Darroudi, M. Green chemical approach for the synthesis of SnO2 nanoparticles and its application in photocatalytic degradation of Eriochrome Black T dye. *Optik* **2021**, *242*, 167152.
(55) Vidya, C.; Manjunatha, C.; Chandraprabha, M. N.; Rajshekar, M.; Raj M.A.L, A. Hazard free green synthesis of ZnO nano-photocatalyst using Artocarpus Heterophyllus leaf extract for the degradation of Congo red dye in water treatment applications. *J. Environ. Chem. Eng.* **2017**, *5*, 3172−3180.
(56) Zangeneh, H.; Zinatizadeh, A. A. L.; Habibi, M.; Akia, M.; Hasnain Isa, M. Photocatalytic oxidation of organic dyes and pollutants in wastewater using different modified titanium dioxides: A comparative review. *J. Ind. Eng. Chem.* **2015**, *26*, 1−36.
(57) Liu, J.; Zhang, Q.; Tian, X.; Hong, Y.; Nie, Y.; Su, N.; Jin, G.; Zhai, Z.; Fu, C. Highly efficient photocatalytic degradation of oil pollutants by oxygen deficient SnO2 quantum dots for water remediation. *Chem. Eng. J.* **2021**, *404*, 127146.
(58) Li, Li.; Huang, J.; Li, R.; Chen, P.; Chen, D.; Cai, M.; Liu, G.; Feng, Y.; Lv, W.; Liu, G. Synthesis of a carbon dots modified g-C3N4/SnO2 Z-scheme photocatalyst with superior photocatalytic activity for PPCPs degradation under visible light irradiation. *J. Hazard. Mater.* **2021**, *401*, 123257.
(59) Alkaykh, S.; Mbarek, A.; Ali-Shattle, E. E. Photocatalytic degradation of methylene blue dye in aqueous solution by MnTiO3 nanoparticles under sunlight irradiation. *Heliyon* **2020**, *6*, No. e03663.
(60) Wu, K.; Shi, M.; Pan, X.; Zhang, J.; Zhang, X.; Shen, T.; Tian, Y. Decolourization and biodegradation of methylene blue dye by a ligninolytic enzyme-producing Bacillus thuringiensis: degradation products and pathway. *Enzyme Microb. Technol.* **2022**, *156*, 109999.
(61) Abbasi, S.; Hasanpour, M. The effect of pH on the photocatalytic degradation of methyl orange using decorated ZnO nanoparticles with SnO2 nanoparticles. *J. Mater. Sci.: Mater. Electron.* **2017**, *28*, 1307−1314.
(62) Cai, R.; Zhang, B.; Shi, J.; Li, M.; He, Z. Rapid Photocatalytic Decolorization of Methyl Orange under Visible Light Using VS4/Carbon Powder Nanocomposites. *ACS Sustain. Chem. Eng.* **2017**, *5*, 7690−7699.
(63) Adeel, M.; Saeed, M.; Khan, I.; Muneer, M.; Akram, N. Synthesis and Characterization of Co-ZnO and Evaluation of Its Photocatalytic Activity for Photodegradation of Methyl Orange. *ACS Omega* **2021**, *6*, 1426−1435.

https://doi.org/10.1021/acsomega.1c07099
ACS Omega 2022, 7, 15423−15438